First results of SO_2 columns from FY3F/OMS instrument observations

Huanhuan Yan[1], Andreas Richter[2], Xingying Zhang[1]*, Anja Schönhardt[2], Thomas Visarius[2]

[1]Key Laboratory of Radiometric Calibration and Validation for Environmental Satellites, National Satellite Meteorological Center (National Center for Space Weather), Innovation Center for FengYun Meteorological Satellite, Beijing, 100081, China.
[2]Institute of Environmental Physics (IUP-UB), University of Bremen, Bremen, 28359, Germany.

Correspondence to: Xingying Zhang (zxy@cma.gov.cn)

Abstract. Atmospheric SO_2 has a significant impact on the urban environment and on global climate. Remote sensing provides an unprecedented tool for the continuous and real-time monitoring of atmospheric SO_2 from volcanic eruptions and anthropogenic emissions. The Ozone Monitoring Suite (OMS) onboard the Chinese FENGYUN-3F (FY-3F) satellite launched in August 2023 is a new hyperspectral UV-VIS instrument in the FY-3 family of satellites, aiming to obtain information about atmospheric trace gases. In this study, we use the OMS Nadir (OMS-N) top-of-atmosphere (TOA) measurements and Differential Optical Absorption Spectroscopy (DOAS) inversion to for the first time retrieve global SO_2 columns from these measurements. Based on the characteristics of the OMS instrument and the performance of its L1 data, specific schemes including solar spectrum selection, spectral soft calibration, and background offset correction were developed to effectively reduce along-track stripes and across-track asymmetry found in the initial OMS SO_2 retrievals. The accuracy of FY-3F/OMS SO_2 retrievals was evaluated by comparing them with the DOAS and COvariance-Based Retrieval Algorithm (COBRA) SO_2 products from the TROPOspheric Monitoring Instrument (TROPOMI) onboard Copernicus Sentinel-5 Precursor (Sentinel-5P) over three typical areas: clean oceanic regions, volcanic eruption regions, and anthropogenic emission regions. The results indicate that the OMS SO_2 retrievals exhibit good stability over clean oceanic regions, successfully capture volcanic SO_2 plumes, and effectively detect the elevated SO_2 columns from anthropogenic emissions in regions such as the Middle East, Eastern India, and Northern Russia. Air mass factor (AMF) uncertainty remains the primary error source of this first version of OMS SO_2 retrievals. This study is the first to present SO_2 retrievals from FY3F/OMS observations, which is crucial for a comprehensive understanding of OMS's capability in SO_2 retrievals.

1 Introduction

Sulfur dioxide (SO_2) is a short-lived trace gas in the atmosphere that affects regional air quality and global climate change. SO_2 is primarily released by anthropogenic activities (e.g., smelting of sulfur ore, combustion of coal, the oil and gas industry, emissions of motor vehicles) and natural phenomena (e.g., volcanic and biological processes) (Finlayson-Pitts and Pitts Jr, 1999; Cullis and Hirschler, 1980; Seinfeld and Pandis, 2016). SO_2 injection from a volcanic eruption can reach up to

带格式的: 下标

删除的内容: Retrieval of SO_2 columns from FY3F/OMS instrument observations

the upper troposphere/lower stratosphere, not only affecting global climate but also posing a threat to aviation, along with volcanic ash. Through reaction with hydroxide and water, atmospheric SO_2 can be rapidly converted into sulfate aerosols. These aerosols both scatter and absorb solar and terrestrial radiation, affecting the radiation balance of the atmosphere (cooling or warming effect) (Twomey, 1977). Sulfate particles formed from anthropogenic SO_2 emissions not only influence atmospheric visibility in the boundary layer but also contribute to acid rain which in turn damages ecosystems.

Satellite remote sensing offers the advantages of near global coverage, short-term periodic observation capabilities, and continuous spatial coverage. Due to the strong absorption characteristics of SO_2 in the ultraviolet (UV) spectrum, especially in the 300–400 nm wavelength range, atmospheric SO_2 information can be obtained from the reflected TOA radiance spectrum. Since the first UV-based satellite observation of large amounts of SO_2 from the El Chichón volcanic eruption in 1982 by TOMS (Krueger, 1983), hyperspectral UV satellite instruments have been used to quantitatively monitor the spatial and temporal distribution of SO_2 concentrations and diffusion trends before and after volcanic eruptions. This compensates for the limitations of ground-based measurements, such as the high cost of dense in-situ observation networks and instrument maintenance (Krueger, 1983; Carn et al., 2005; Carn et al., 2007; Carn et al., 2009).

With the launch of a series of hyperspectral UV detection instruments, including the Global Ozone Monitoring Experiment (GOME) (Burrows et al., 1999; Khokhar et al., 2005; Eisinger and Burrows, 1998), the Scanning Imaging Absorption Spectrometer for Atmospheric Cartography (SCIAMACHY) (Gottwald and Bovensmann, 2010; Richter et al., 2006), the Ozone Monitoring Instrument (OMI) (Levelt et al., 2006), the Global Ozone Monitoring Experiment-2 (GOME-2) (Heue et al., 2010; Munro et al., 2006; Richter, 2009), the Ozone Mapping and Profiler Suite (OMPS) (Yang et al., 2013; Flynn et al., 2006), TROPOMI (Theys et al., 2019; Voors et al., 2017; Veefkind et al., 2012), and the Environmental Trace Gas Monitoring Instrument (EMI) (Chen et al., 2021; Zhao et al., 2020; Yan et al., 2021), satellite detection has been widely applied to monitor global SO_2 variations and to support research on climate change, atmospheric chemistry, and the atmospheric environment.

FY3F/OMS is a newly launched Chinese UV-VIS hyperspectral sensor that provides global observations with 7 km × 7 km spatial resolution at nadir and a morning overpass time. For a thorough understanding of the OMS SO_2 product, this study presents OMS SO_2 retrievals by using the OMS measurements and DOAS inversion, and compares them with TROPOMI DOAS and TROPOMI COBRA SO_2 products over clean oceanic regions, volcanic eruption regions, and anthropogenic emission regions. This paper is organized as follows. Section 2 gives a brief introduction to the FY3F/OMS instrument. Section 3 describes the detailed procedures used to retrieve the SO_2 columns from FY3F/OMS observations, including solar spectrum selection, spectral soft calibration, SO_2 slant column density (SCD) retrieval, background offset correction, and the simplified approach for AMF calculation used. Section 4 provides the OMS SO_2 column results, followed by comparisons with the TROPOMI DOAS and TROPOMI COBRA SO_2 products. Section 5 discusses error sources of OMS SO_2 retrievals, including the instrument-related errors and DOAS SCD spectral fitting errors in OMS SO_2 SCD retrievals, errors introduced by the simplified AMF approach taken, and the residual errors after background offset correction. The last section summarizes the main results and offers conclusions, along with suggestions for future improvements.

2 The FY3F/OMS Instrument

The FY-3F satellite, the 21st in China's FengYun series, was successfully launched on August 3, 2023. It operates in a sun-synchronous orbit at an altitude of 836 km, with a descending node equatorial overpass time of 10:00 AM. Equipped with 10 advanced atmospheric instruments, FY-3F is designed to provide high-quality data for weather forecasting, climate monitoring, and environmental research, contributing significantly to global meteorological and environmental observations.

The Ozone Monitoring Suite (OMS) onboard FY-3F satellite is a new instrument in the FY-3 family of satellites. It has two observation modes: Nadir (OMS-N) and Limb (OMS-L) (Wang et al., 2024). While OMS-L provides information on the vertical distribution of O_3, OMS-N is mainly used to obtain column information on trace gases such as O_3, NO_2, SO_2, and HCHO, and aerosols, as well as vertical profiles of O_3. OMS-N operates using a push-broom observation technique to obtain daily global measurements, with a wide Field of View (FOV) of 112 °, covering three spectral bands: UV1 (250-300 nm), UV2 (300-320 nm), and VIS (307-493 nm). To enhance the signal-to-noise ratio (SNR) of the original detector rows, sets of 16 pixels are averaged to yield 58 spatial rows in the UV1 band, and four pixels are averaged to acquire 238 spatial rows in the UV2 and VIS bands, respectively (Wang et al., 2024). The OMS-N VIS band (307-493 nm) was used for the retrieval of OMS SO_2 columns in this study. It has a high spatial resolution of 7 km x 7 km at the nadir point, with a spectral resolution of 0.5-0.6 nm (Table 1). FY3F/OMS data can be downloaded from the website http://data.nsmc.org.cn/DataPortal/en/home/index.html.

Table1. The main characteristics of the FY3F/OMS-N instrument

Parameter	Nadir column measurement	Nadir profile measurement
Spectral range	VIS: 307~493nm	UV1:250~300nm UV2: 300~320nm
Spectral resolution	0.5~0.6nm	UV1: ~1.0nm UV2: ~0.5nm
Spectral accuracy	0.01nm	0.05nm
Spatial resolution at nadir point	7 km x 7 km	UV1: 21 km x 28 km UV2: 7 km x 7 km
Atmospheric products	O_3, NO_2, SO_2, HCHO, AOD, cloud fraction and pressure	O_3 profile
Field of view	112 °	
Orbit observation	polar sun synchronous morning orbit	
Orbit altitude	836 km	
Equator crossing time	10:00 AM	
Duty Cycle	Daytime only	
Revisit Time:	24 hours	

3 SO_2 column retrievals from FY3F/OMS

The SO_2 retrieval from FY3F/OMS mainly involves the following steps. (1) Firstly, the OMS-N L1 earth radiance is normalized to the Earth-Sun distance of 1AU, while the solar irradiance is obtained by convolving the Total and Spectral Solar Irradiance Sensor (TSIS) Hybrid Solar Reference Spectrum (HSRS) (Coddington et al., 2021) (See section 3.1 for more information) with the Instrument Spectral Response Function (ISRF) of OMS-N. (2) Secondly, the 312-326 nm region is chosen as the retrieval fitting window of the OMS SO_2 column. (3) Thirdly, spectral soft calibration is performed using the absorption peaks and valleys of the solar reference spectrum. (4) Fourthly, the cross sections of SO_2 and O_3 in 312-326 nm are convolved with the ISRF. (5) Fifthly, the Ring spectrum is calculated using the SCIATRAN Radiative Transfer Model (Rozanov et al., 2005). (6) Sixthly, SO_2, O_3 and Ring cross-sections together with a third-order polynomial are used in the DOAS fitting process to obtain the SCD of OMS SO_2. (7) Seventhly, the AMF is applied to get vertical column density (VCD). (8) Finally, a specific correction scheme for OMS background offset is applied to effectively reduce along-track stripes and across-track asymmetries in the initial OMS SO_2 retrievals. It should be noted that, due to the current unavailability of synchronized and reliable OMS cloud and aerosol products, the effects of clouds and aerosol on SO_2 retrievals were not considered in this study. For the OMS SO_2 product, it is recommended to use retrieval results with a solar zenith angle smaller than 70 °, near-nadir and cloud-free pixels.

3.1 Solar irradiance

Using the satellite measured solar irradiance for the DOAS SO_2 retrieval can effectively reduce instrument-related errors. However, due to the degradation and non-uniformity of the diffuser plate of OMS, the OMS L1 irradiance measurements experienced increasing errors after launch, especially in the shortwave UV region (for more information see section 5.1). Therefore, in this study the TSIS HSRS hybrid solar reference spectrum (Coddington et al., 2021) was used for OMS SO_2 retrievals instead of OMS daily measured solar irradiance. The TSIS HSRS hybrid solar reference spectrum was developed by normalizing high spectral resolution solar datasets to the absolute irradiance scale of the TSIS-1 Spectral Irradiance Monitor (SIM) and the CubeSat Compact SIM (CSIM). The high spectral resolution solar data are sourced from the Air Force Geophysical Laboratory (AFGL) ultraviolet solar irradiance balloon observations, the ground-based Quality Assurance of Spectral Ultraviolet Measurements in Europe Fourier Transform Spectrometer (QASUMEFTS) solar irradiance observations, the Kitt Peak National Observatory (KPNO) solar transmittance atlas, and the semi-empirical Solar Pseudo Transmittance Spectrum (SPTS) atlas. The TSIS-1 HSRS spans 202–2730 nm at 0.01 to ~0.001 nm spectral resolution with uncertainties of 0.3% between 460 and 2365 nm and 1.3% at wavelengths outside that range (Coddington et al., 2021).

The TSIS HSRS hybrid solar reference spectrum was convolved with the OMS-N ISRF to match the spectral characteristics of OMS radiance. The FY3F/OMS-N ISRF was determined using tunable laser scanning with a step size of 0.02 nm,

providing the relative response of each detector pixel on the focal plane arrays to monochromatic illumination (Wang et al., 2024). It varies in both the spectral and spatial dimensions of the two large array detectors. The shape of the FY3F/OMS-N ISRF exhibits a flat top in the central peaks because OMS-N adopts a stereoscopic slit observation mode (Wang et al., 2024). The TSIS HSRS hybrid solar reference spectrum provides high accuracy solar irradiances, but as it was not measured with the OMS-N instrument, any calibration issues in the radiances do not cancel in the DOAS retrieval. Therefore, its use may lead to systematic overestimation or underestimation in the retrieved SO_2 columns, as well as along-track stripes, which cannot be fully corrected through post-processing algorithms.

3.2 Spectral soft calibration

Before the DOAS fitting retrieval, spectral soft calibration was applied to the FY3F/OMS radiance data. Spectral soft calibration can correct wavelength shifts caused by factors such as instrument drift, temperature fluctuations, radiation effects, and nonlinear effects, using known absorption features to adjust the initial L1 data. The spectral soft calibration process ensures the accuracy and consistency of the OMS radiances, which is essential for accurate SO_2 retrieval and for minimizing the impact of calibration errors on the SO_2 retrieval.

The spectral soft calibration is performed using the peaks and valleys of the TSIS HSRS hybrid solar reference spectrum (Van Geffen and Van Oss, 2003; Coddington et al., 2021). The detailed process includes: 1) Selecting the high-resolution hybrid solar reference spectrum (Coddington et al., 2021), and convolving the reference spectrum with the slit function of the FY3F/OMS instrument; 2) Fitting the ratio of the solar reference spectrum to the observed radiance spectrum with a low-order polynomial to enhance the observed radiance spectrum; 3) For each observed radiance spectrum in the SO_2 fitting window, Gaussian peak-finding is performed to match the peak position of a set of Fraunhofer lines with their corresponding wavelengths. A least-squares method is used to fit the spectral line wavelengths and the peak position number data with a third-order polynomial, generating a spectral calibration equation for each observed pixel. Then the spectral soft calibration of the FY3F/OMS radiance is realized by using the above spectral calibration equation.

删除的内容: was

3.3 DOAS SCD retrieval

3.3.1 SO_2 fitting window

The selection of the retrieval fitting window is crucial for the accuracy of OMS SO_2 retrievals, which significantly affect OMS capability in monitoring SO_2 from volcanic and anthropogenic sources. A suitable fitting window helps to reduce the impact of interfering gases (O_3), to enhance the SO_2 information content in the satellite signal and to obtain reliable SO_2 results. In this study, the 312-326 nm fitting window was chosen for the SO_2 retrieval from OMS observations. This is mainly based on the following considerations:

带格式的: 字体: (默认) Times New Roman, (中文) Times New Roman

删除的内容: is

(1) Firstly, in the wavelength range 310-330 nm, although SO_2 has stronger absorption at shorter wavelengths (Fig. 1) which would make it preferable, satellite measurements at shorter wavelengths have lower SNR, and in the case of volcanic SO_2

emission, the TOA reflected radiances are prone to saturation which leads to underestimation of volcanic SO_2. Therefore, it is not appropriate to select the fitting window with the strongest SO_2 absorption for SO_2 retrieval.

(2) Secondly, longer UV wavelengths, due to the weaker absorption of SO_2, tend to introduce more noise into the retrieval of the SO_2 column. This is because the weaker absorption may make it more difficult to accurately distinguish the SO_2 absorption information from background noise and interference of O_3 absorption, especially in the case of low SO_2 emissions from anthropogenic sources.

(3) Thirdly, selecting the 312–326 nm fitting window makes the OMS SO_2 product consistent with the widely used TROPOMI SO_2 product (Theys et al., 2017). However, in this study, we did not adopt a strategy with multiple fitting windows for different SO_2 concentration conditions as is used in the TROPOMI product.

(4) Finally, in order to demonstrate the advantage of the 312-326 nm fitting window for OMS SO_2 retrievals, comparisons were conducted between SO_2 retrievals from different fitting windows over the Sundhnúkur volcano and its surrounding clean region for August 23, 2024 (Figs. 2, 3, and 4). Note that negative values often appear in SO_2 retrievals, and small negative values can indicate low SO_2 emissions in clean areas. In this study, all SO_2 retrievals greater than -10 DU are selected for comparison to exclude obvious outliers. The details of the comparisons are described below.

The main fitting windows and retrieval algorithms used in the literature for SO_2 retrievals based on ultraviolet hyperspectral satellite measurements are listed in Table 2. The OMS SO_2 columns retrieved using these different fitting windows are shown in Figs. 2, 3, and 4. Note that due to the DOAS algorithm generally using a continuous UV fitting window for SO_2 retrieval, the OMS SO_2 results from BRD four discrete wavelengths (310.8, 311.9, 313.2, and 314.4 nm) at absorption peak and valley (Krotkov et al., 2006) are not included in this study. It also should be noted that, since the OMS VIS spectral band starts from 307 nm and the OMS UV2 spectral range from 300 nm to 320 nm requires further calibration, the 300-335 nm fitting window used by the EISF algorithm was not tested in this section.

As shown in Figs. 2 and 3, the retrieval results of SO_2 columns from the 315–327 nm, 325–335 nm, 360–390 nm, 317.8–333 nm, and 315–326 nm fitting windows are first excluded due to the large errors observed in the clean regions (e.g., OMS cross-track positions 1-150). The retrieval results from the 308–333 nm fitting window are also excluded because the results are relatively lower in the volcanic region than those from the other fitting windows. Finally, according to the retrieval results of SO_2 columns in Fig. 4, the retrieval results from the 312–326 nm and 312–330 nm fitting windows show higher and similar values in the volcanic region. Additionally, in the clean regions (cross-track positions 1-150), both 312–326 nm and 312–330 nm fitting windows exhibit lower and similar standard deviations and mean values. Therefore, considering all the above reasons and to be consistent with the TROPOMI DOAS SO_2 product, the 312–326 nm fitting window was selected for OMS SO_2 retrieval in this study.

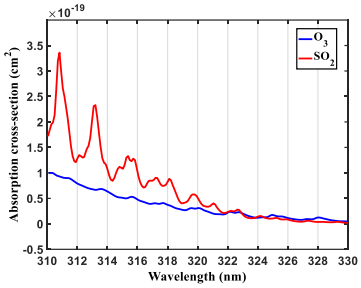

Figure 1: Absorption cross sections of SO_2 and O_3 in the wavelength range 310-330 nm (Bogumil et al., 2003).

180

Table 2. Retrieval algorithms and fitting windows used for SO_2 retrieval from UV-VIS hyperspectral satellite measurements

Instruments	Retrieval algorithms	Fitting windows
SCIAMACHY	DOAS	315–327 nm (Platt and Stutz, 2008; Richter et al., 2006)
OMI	Principal Component Analysis (PCA)	310.5–340 nm (Li et al., 2013)
	Iterative Spectral Fitting (ISF)	317.8–333 nm (Yang et al., 2009)
	Extended Iterative Spectral Fitting (EISF)	300–335 nm (Yang et al., 2010)
	Band Residual Difference (BRD)	Four discrete wavelengths (310.8, 311.9, 313.2, and 314.4 nm) (Krotkov et al., 2006)
GOME-2	Optimal Estimation (OE)	312–330 nm (Nowlan et al., 2011)
	DOAS	315–326 nm (Fioletov et al., 2013)
OMPS	Iterative Spectral Fitting (ISF)	308–333 nm (Yang et al., 2013)
TROPOMI	DOAS	312–326 nm, 325–335 nm, and 360–390 nm (Theys et al., 2017)
	COBRA	310.5–326 nm (Theys et al., 2021)

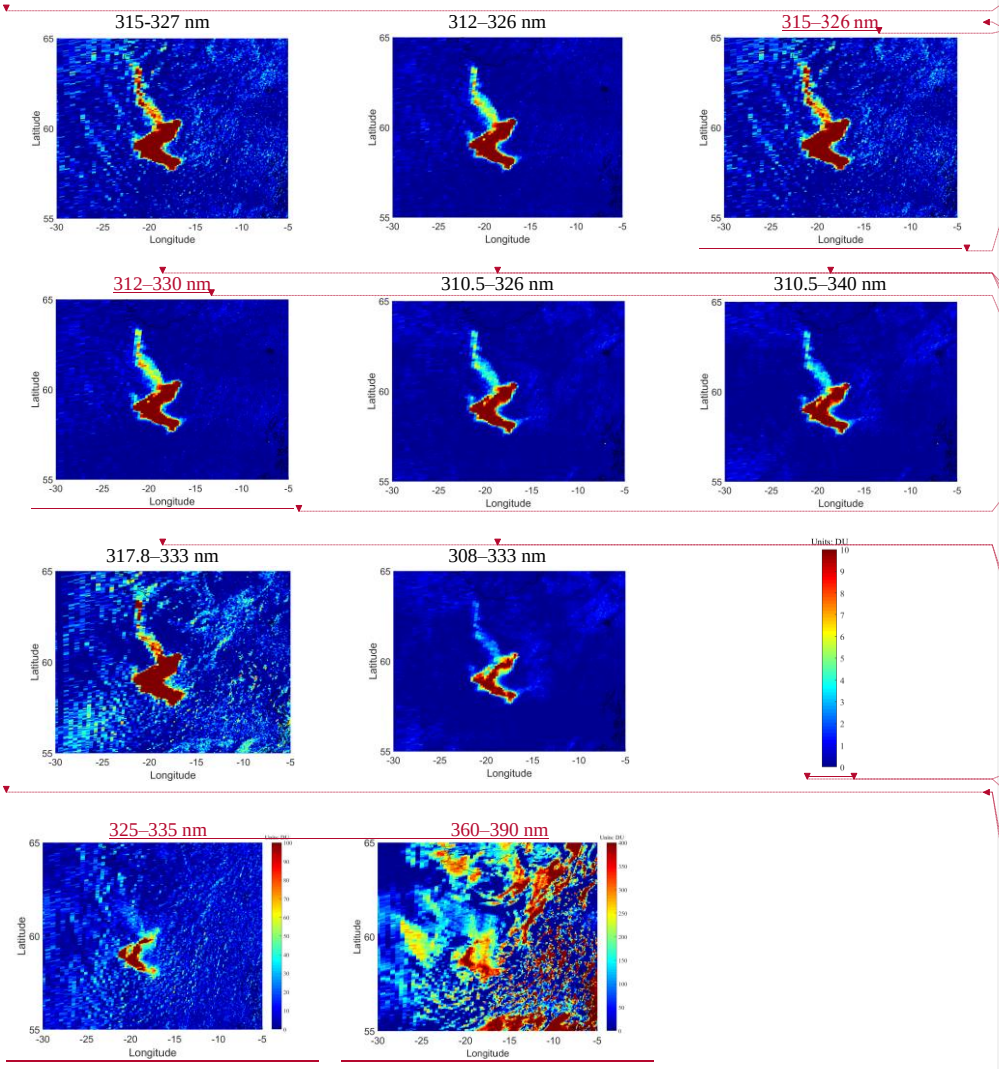

Figure 2: SO_2 retrievals from different fitting windows over the Sundhnúkur volcano on August 23, 2024 (OMS orbit 20240823_1036). DU=Dobson Units, 1DU=2.69×10[16] molecules/cm^2.

删除的内容：.

.

删除的内容: 325–335 nm

带格式表格

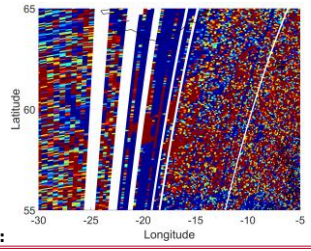

删除的内容:

删除的内容：.

删除的内容：.

删除的内容：.

删除的内容: 360–390 nm

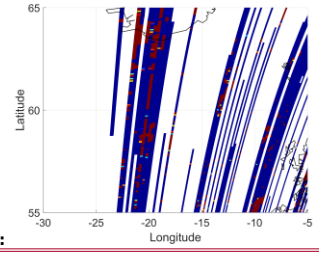

删除的内容:

删除的内容：.

删除的内容：.

删除的内容：.

.

312–330 nm .

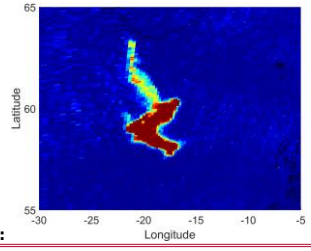

删除的内容:

删除的内容：.

.

...

带格式的: 行距: 最小值 0 磅

删除的内容: The missing pixels in the figures are caused by inversion failures resulting in Nan values.

删除的内容：.

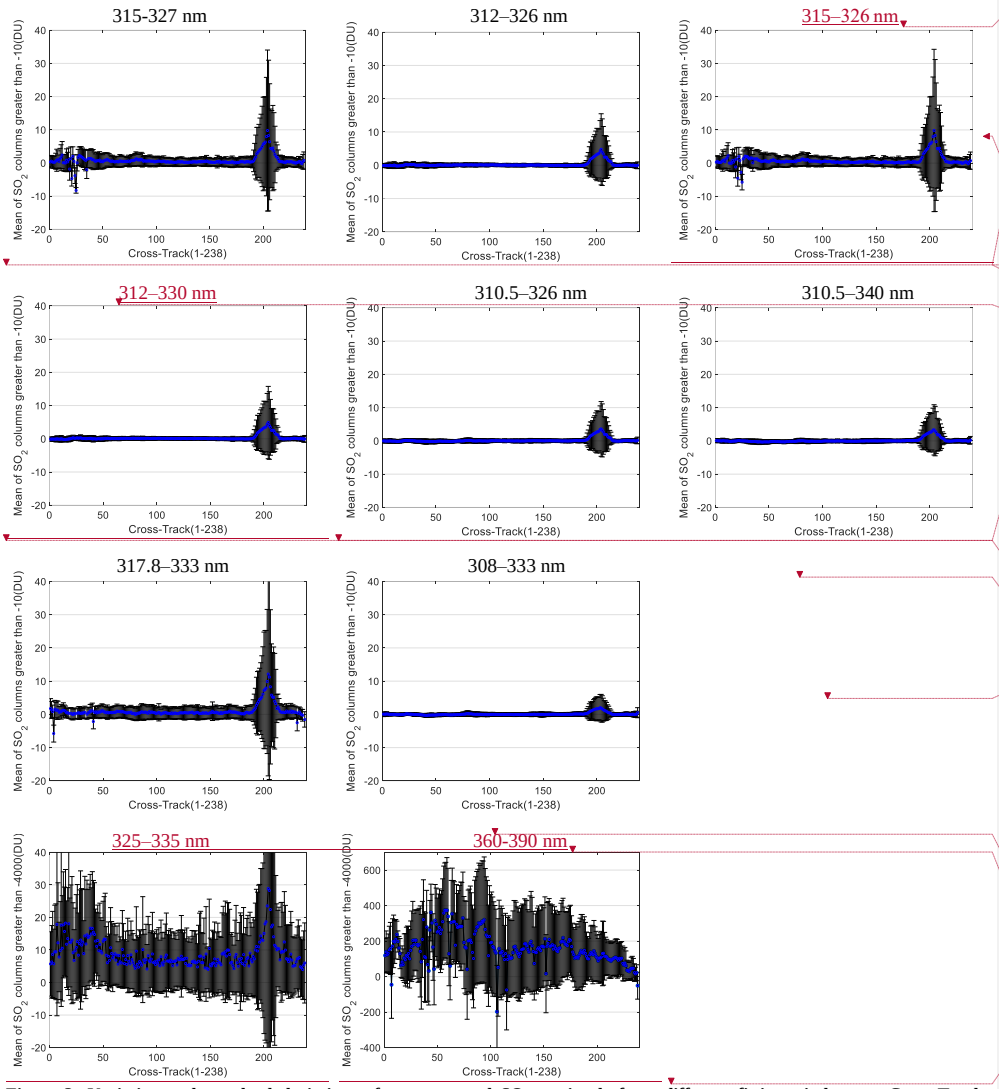

Figure 3: Variation and standard deviations of row-averaged SO_2 retrievals from different fitting windows at Cross-Track positions over Sundhnúkur volcano and its surrounding region on August 23, 2024, OMS rows from 700 to 870 of orbit 20240823_1036.

删除的内容: 325–335 nm

删除的内容:

带格式表格

删除的内容: .

删除的内容: 360-390 nm

删除的内容:

删除的内容: .

删除的内容: 312–330 nm

删除的内容:

删除的内容: .

删除的内容: 315–326 nm

删除的内容:

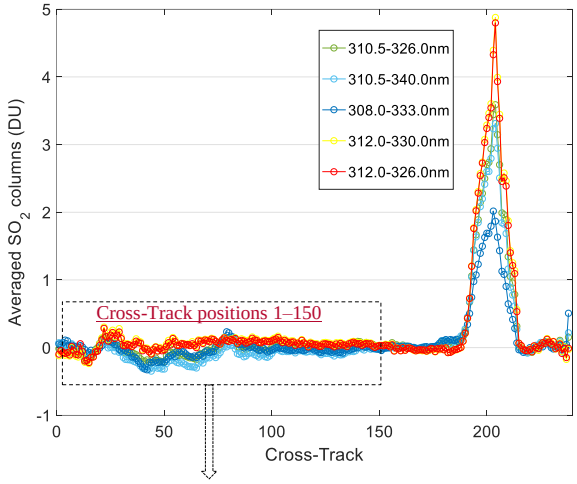

Fitting window (nm)	Standard deviation (DU)	Mean value (DU)
312–326	0.08	0.04
310.5–326	0.09	-0.03
310.5–340	0.1	-0.1
308–333	0.09	-0.04
312–330	0.09	0.06

Figure 4: Row-averaged SO_2 retrievals from OMS rows 700 to 870 of orbit 20240823_1036 by using different spectral fitting windows.

3.3.2 The Ring effect

The Ring effect refers to the phenomenon that the Fraunhofer lines present in the solar spectrum from absorption in the solar atmosphere by elements such as potassium and calcium are partially filled in spectra of scattered light taken in the Earth's atmosphere (Grainger and Ring, 1962). For the Ring effect in satellite-observed spectra, the primary source is the rotational Raman scattering of N_2 and O_2 molecules in the atmosphere, which redistributes photon energy and leads to the filling-in of Fraunhofer and atmospheric absorption lines (Sioris and Evans, 1999; Fish and Jones, 1995; Chance and Spurr, 1997; Vountas et al., 1998). For OMS SO_2 column retrievals using the DOAS method, the Ring effect is an important factor

带格式的: 右侧: 1.69 厘米
带格式的: 居中
带格式表格
带格式的: 字体: (中文) +中文正文 (宋体), (中文) 中文(中国)
带格式的: 居中
带格式的: 字体: (中文) +中文正文 (宋体), (中文) 中文(中国)
带格式的: 字体: (中文) +中文正文 (宋体), (中文) 中文(中国)
带格式的: 居中
带格式的: 字体: (中文) +中文正文 (宋体), (中文) 中文(中国)
带格式的: 字体: (中文) +中文正文 (宋体), (中文) 中文(中国)
带格式的: 字体: (中文) +中文正文 (宋体), (中文) 中文(中国)
带格式的: 居中
带格式的: 居中
带格式的: 居中
带格式的: 右侧: 1.69 厘米
删除的内容: For Cross-Track positions 1–150, the standard deviations and mean values of SO_2 retrievals are 0.08 DU and 0.04 DU for the 312–326 nm window, 0.09 DU and -0.03 DU for 310.5–326 nm, 0.10 DU and -0.10 DU for 310.5–340 nm, 0.09 DU and -0.04 DU for 308–333 nm, and 0.09 DU and 0.06 DU for 312–330 nm, respectively.

influencing the accuracy of retrieval results due to the strong Ring spectrum in the UV wavelength band (Fig. 5). Taking the OMS 20240823_1036 orbit as an example, after including the Ring spectrum into the DOAS retrieval, the spectral fitting residual RMSE for most OMS pixels decreases by approximately 0.004 to 0.01.

In this study, during the OMS SO_2 DOAS retrieval, the Ring effect is considered as a pseudo-absorption effect, and the Ring spectrum calculated using the SCIATRAN radiative transfer model (Rozanov et al., 2005) is included as a pseudo-absorber in the spectral fitting process, as shown in Equation (1).

$$-\ln\frac{\pi*I(\lambda)}{F(\lambda)*\cos(SZA)} = \sigma_{SO_2}(\lambda)\times SCD_{SO_2} + \sigma_{O_3}(\lambda)\times SCD_{O_3} + \sigma_{Ring}(\lambda)\times C_{Ring} + P(\lambda) + E(\lambda) \quad \text{(Eq. 1)}$$

Where $I(\lambda)$ and $F(\lambda)$ are the satellite-observed radiance and the solar reference spectrum convolved with the OMS ISRF, SZA is the Solar Zenith Angle, $\sigma_{SO_2}(\lambda)$ and $\sigma_{O_3}(\lambda)$ are the absorption cross-section of SO_2 and O_3, SCD_{SO_2} and SCD_{O_3} are the slant column density of SO_2 and O_3, $\sigma_{Ring}(\lambda)$ is the Ring spectrum calculated using the SCIATRAN model and convolved with the OMS ISRF, C_{Ring} is the Ring absorption coefficient determined by the fitting, $P(\lambda)$ is a low-order polynomial, and $E(\lambda)$ is the error term. Note that in this study the SCIATRAN Ring spectrum for typical atmospheric conditions and observational geometry (SZA=30 °, Viewing Zenith Angle (VZA)=0 °, Relative Azimuth Angle (RAA)=0 °, surface reflectance (AS)=0.05, surface height above sea level (HS) (also referred to as terrain height)=0 km, ozone column=275 DU, clear sky) is used in the DOAS fitting for all OMS measurements, without considering the variations of the Ring spectrum due to different atmospheric conditions and viewing geometries.

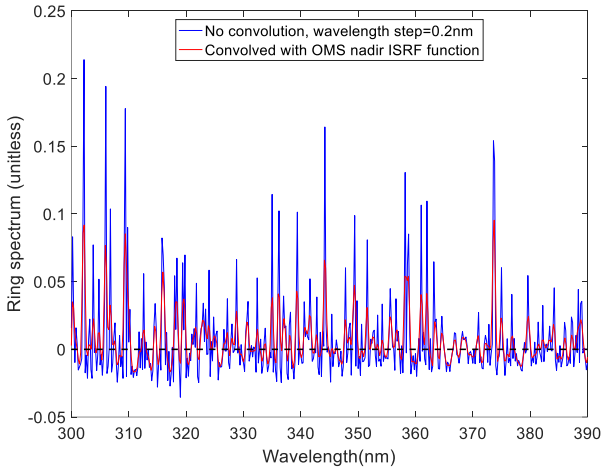

Figure 5: Ring spectrum calculated with the SCIATRAN model, convolved with the OMS ISRF. SCIATRAN forward settings are SZA=30 °, VZA=0 °, RAA=0 °, Surface albedo=0.05, Ozone column=275 DU, Clear sky.

3.3.3 Spectral fitting

The retrieval of the FY3F/OMS SO_2 SCD is primarily based on the classical DOAS theory (Platt and Stutz, 2008). It utilizes Beer-Lambert's law and the satellite hyperspectral radiance observations in the UV fitting window to derive the SO_2 SCD along the entire photon path. First, the absorption cross-section of SO_2 and O_3, measured under specific laboratory conditions with a higher spectral resolution and different sampling points than those of OMS observations, are convolved with the OMS ISRF to match the spectral resolution of the OMS instrument. Secondly, atmospheric extinction is divided into two components: a fast-varying part with wavelength, typically associated with narrow absorption features of SO_2 and O_3, and a slow-varying part with wavelength, related to broad spectral features of absorption and atmospheric scattering processes such as Rayleigh and Mie scattering. A low-order polynomial is used to remove the slow-varying components, while preserving the fast-varying part related to SO_2 and O_3 absorption. Finally, the slow-varying part of satellite-observed TOA reflectance (the ratio of L1 radiance to irradiance data) are removed by subtracting a low-order polynomial, and the atmospheric SO_2 SCD is obtained through least-squares fitting.

Table 3. Parameter settings for the retrieval of FY3F/OMS SO_2 SCD

Parameter	FY3F/OMS SO_2 DOAS settings
Retrieval fitting window	312－326 nm
Solar irradiance	TSIS HSRS hybrid solar reference spectrum (Coddington et al., 2021)
Cross-sections	SO_2 273K (Bogumil et al., 2003) O_3 223K (Bogumil et al., 2003)
Ring effect	Ring spectrum calculated using the SCIATRAN model at SZA=30 °, VZA=0 °, RAA=0 °, AS=0.05, Clear sky (Rozanov et al., 2005)
Polynomial	3^{th} order
Background offset correction	Iterative and sliding correction scheme

3.4 Background offset correction

The retrieval accuracy of SO_2 columns from satellite measurements is usually affected by spectral and radiometric calibration errors, which are difficult to remove from L1 radiance data and result in systematic biases in the retrieval results, such as along-track stripes and cross-track asymmetry (Boersma et al., 2004). In addition, due to the low SNR of measurements in the fitting window, the weak SO_2 absorption information included in the TOA reflected radiance, and the interference from strong O_3 absorption in the fitting window, the OMS SO_2 retrievals tend to be systematically overestimated or underestimated over the whole orbit. These systematic biases in the retrieval results of SO_2 columns are mixed with the absorption information of SO_2 and limit the applicability of the OMS SO_2 product. Therefore, it is necessary to apply a background offset correction to reduce these systematic biases in the retrieved SO_2 columns. The reference region method (Khokhar et al., 2005; Richter et al., 2006) was used to correct the background offsets, which are latitude-dependent and related to the cross-track position. This method selects retrieval values over a reference region (e.g., clean oceanic Pacific regions, assumed to be areas with no SO_2) as the background area. The SO_2 retrievals are then adjusted by subtracting the background offsets of the same latitude over the ocean. Yang proposed the sliding median correction method (Yang et al., 2007) and applied it to the OMI SO_2 product. This method performs averaged sampling within a sliding window centered on the pixel (selecting pixels with values less than 2 DU) to get background offsets for each row of pixels. With the sliding window method, the cross-track and along-track biases varying with time and location can be effectively eliminated.

For OMS SO_2 retrievals, based on the above background offset correction methods, we developed an improved iterative sliding correction scheme to avoid seam problems due to discontinuous integration times within the same orbit. The details of the background offset correction used for OMS SO_2 retrievals are as follows.

(1) Firstly, based on the integration time of FY3F/OMS L1 data, the orbital data is divided into several data blocks corresponding to different integration times. For each data block, the mean vector (V0) at each cross-track position is estimated using all valid pixels within the block (i.e., pixels with normal L1 data, as indicated by the L1 QA quality flag). Each scan line within the data block is processed by subtracting V0 from the SO_2 retrievals of each scan line to obtain the initially corrected SO_2 columns.

(2) Secondly, based on the initially corrected SO_2 columns, the predefined SO_2 threshold (2 DU), and the sliding window, the mean vector V1 for cross-track positions within each sliding window is estimated. The initially corrected SO_2 columns are then processed by subtracting V1 to obtain the double-corrected SO_2 columns. Note that the size of the sliding window varies with the satellite's spatial resolution. In this study, for the FY3F/OMS with nadir resolution of 7 km×7 km, the sliding window is set to 200 scan lines. It is worth noting that there is a trade-off between the size of the sliding window and the effectiveness of the offset correction: too big a window might result in poor offset correction, while too small a sliding window might lead to reduction of the SO_2 information contained in the satellite measurements.

(3) Finally, based on the double-corrected SO_2 results, the predefined SO_2 threshold, and the sliding window, an iterative procedure is performed until the relative deviation between the results of the two consecutive corrections is less than or equal to 5%.

3.5 AMF

The reflected radiance detected by the satellite instrument contains information of trace gases integrated along the slant observation path. From the reflected radiance and above DOAS spectral fitting, the SO_2 SCD can be derived; however, the SCD is not suitable for the application of satellite-derived SO_2 in monitoring global climate change and air pollution, as it represents the SO_2 column along the slant path, which is influenced by the observation geometry and atmospheric conditions. The SCD can be converted to VCD using AMF=SCD/VCD (Palmer et al., 2001), which represents the relative length of the mean slant path at a certain wavelength for photons interacting with a certain absorber in the atmosphere relative to the vertical path (Lorente et al., 2017).

The AMF is typically computed as the weighted average of altitude-dependent Box-AMFs (equivalent to scattering weights) across all layers, with the weights determined by the SO_2 distribution in each layer (Eq. 2) (Chen et al., 2009; Wagner et al., 2007; Palmer et al., 2001; Boersma et al., 2004):

$$AMF = \sum_i \text{Box-AMF}_i \times \frac{c_i \cdot \Delta h_i}{\sum_j c_j \cdot \Delta h_j} \quad \text{(Eq. 2)}$$

Where c_i represents the SO_2 number density in the i-th layer, and Δh_i denotes the thickness of that layer. Box-AMFs quantify the contribution of each atmospheric layer to the total AMF and allows for flexible updates of AMF with new SO_2 profiles, eliminating the procedure of rebuilding the AMF lookup table.

However, due to the difficulty in obtaining accurate and satellite-synchronized global SO_2 profiles, we adopted a simplified approach that uses two constant AMF values representative for typical conditions for the OMS SO_2 conversion from SCD to VCD in this study. One is AMF=1 for clean regions and non-ice/snow-covered areas influenced by anthropogenic sources and volcanic eruptions, while the other is AMF=2 for the ice/snow-covered areas. These two AMF constants are approximate values derived using the SCIATRAN Box-AMF and a 5 DU anthropogenic SO_2 profile under typical atmospheric and surface conditions (SZA = 32.9 °, VZA = 0 °, RAA = 0 °, AS = 0.05 and 0.5, HS = 0 km, wavelength = 320 nm, a 365 DU midlatitude ozone profile (Sinnhuber et al., 2009), and with the assumption of surface reflectance as isotropic Lambertian equivalent reflector (LER)). Section 5.2 of this study provides a more detailed description of Box-AMF and an error analysis of the AMF.

删除的内容: can be calculated by using Box-AMF from forward radiative transfer model and local SO_2 profile (Chen et al., 2009; Wagner et al., 2007; Palmer et al., 2001; Boersma et al., 2004).

4 Comparison of OMS SO_2 columns with TROPOMI observations

Based on the FY3F/OMS L1 measurements and the retrieval scheme outlined in section 3, global SO_2 columns from FY3F/OMS were retrieved and applied to monitor the SO_2 emissions from volcanic and anthropogenic activities. Evaluating

the accuracy of OMS SO_2 retrievals is challenging, as it is difficult to obtain synchronous and high-quality ground-based or airborne measurements for the validation of OMS SO_2 retrievals. Therefore, in this study, due to its high spatial and spectral resolution in the UV-VIS band and its common use in global SO_2 monitoring, the TROPOMI SO_2 total column product was selected as reference to evaluate the accuracy of OMS SO_2 retrievals (Theys et al., 2019; Wang et al., 2022; Theys et al., 2017; Cofano et al., 2021; Corradino et al., 2024; Fioletov et al., 2020). It should be noted that, in the comparison between OMS and TROPOMI SO_2 results, no filtering for cloud or large SZA was applied to the OMS SO_2 data; instead, all OMS SO_2 retrievals greater than -10 DU were selected for the comparison.

带格式的: 下标

TROPOMI has a local overpass time of 13:30, a spatial resolution of 5.5 km×3.5 km for SO_2 and provides daily global coverage with ~14 orbits per day. TROPOMI SO_2 products from two algorithms are used for comparison: one is the TROPOMI offline L2 orbital SO_2 product from the DOAS algorithm (hereafter referred to as TROPOMI DOAS) (Data source: https://browser.dataspace.copernicus.eu/), and the other is the TROPOMI L3 grid Planetary Boundary Layer (PBL) and 7km SO_2 product from the COBRA algorithm (hereafter referred to as TROPOMI COBRA) (Data source: https://data-portal.s5p-pal.com/products/SO_2cbr.html). The TROPOMI COBRA SO_2 product was developed by Royal Belgian Institute for Space Aeronomy (BIRA), and reduces significantly both the noise and biases present in the current TROPOMI operational DOAS SO_2 retrievals (Theys et al., 2021). The TROPOMI COBRA L3 grid product (0.022 °×0.022 ° equal latitude-longitude grid) was generated using the HARP gridding tool from L2 data applying a Quality Assurance (QA) filter (QA>0.5) to remove low quality data. The quality filtering leads to some gaps in the COBRA data

Figure 6 shows the 15-days averaged global SO_2 SCDs from OMS DOAS and TROPOMI DOAS from November 1st to 15th, 2024. The OMS DOAS SO_2 SCDs were averaged using pixels with SO_2 column greater than -10 DU, whereas the TROPOMI DOAS SO_2 SCDs were averaged using pixels with QA > 0.5. It is worth noting that since negative values often appear in SO_2 retrievals, and small negative values can indicate low SO_2 emissions in clean areas, in this study OMS SO_2 retrievals greater than -10 DU are selected for comparison. As shown in Fig. 6, the OMS and TROPOMI DOAS SO_2 SCDs exhibit generally consistent spatial distributions, both clearly identifying the major global SO_2 emission hotspots. However, there are slight differences between the OMS and TROPOMI DOAS SO_2 SCDs, which may be attributed to differences in observational geometry, overpass time, and algorithmic processing. Further comparisons between OMS, TROPOMI DOAS and TROPOMI COBRA SO_2 columns based on individual orbits are discussed in Sections 4.1, 4.2, and 4.3. The effectiveness of OMS SO_2 retrievals was evaluated by comparing them with TROPOMI over clean oceanic regions, volcanic eruption regions, and anthropogenic emission regions as shown in Fig. 7.

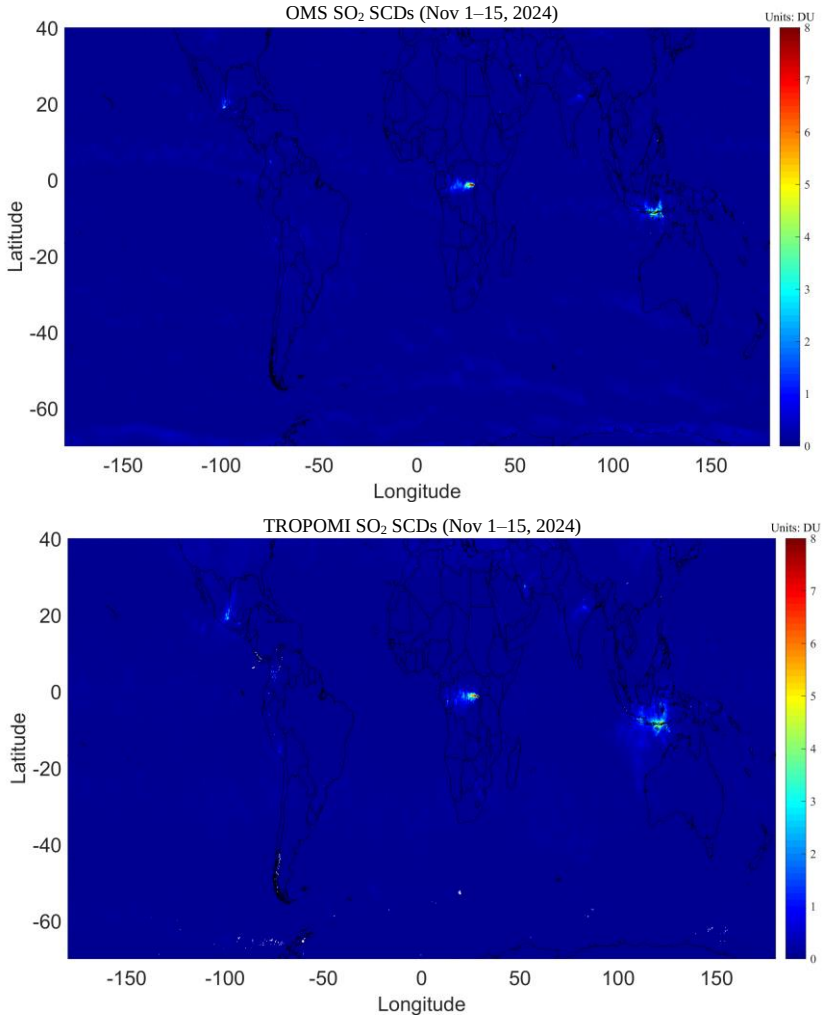

Figure 6: Global maps of averaged SO_2 SCDs from OMS DOAS and TROPOMI DOAS during the period of November 1st to 15th, 2024, 0.2 °×0.2 ° equal latitude-longitude grid. Note that the TROPOMI DOAS SO_2 SCDs are obtained from the product variable 'fitted_slant_columns_win1', corresponding to the 312–326 nm wavelength fitting window.

带格式的：居中

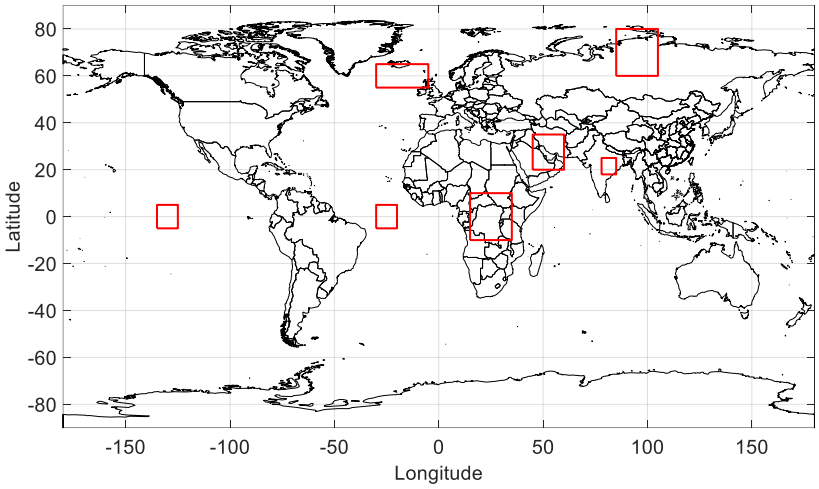

Figure 7: Regions selected for the comparison of OMS and TROPOMI SO_2 columns.

4.1 Comparison over clean oceanic regions

Ideally, the retrieved SO_2 values from satellite observations in clean regions should be close to zero. The scatter of SO_2 columns in clean regions can reflect the reliability and stability of the satellite data and the retrieval algorithm (Krotkov et al., 2008). In this study, two clean oceanic regions, where SO_2 emissions are extremely low and assumed to be zero, were selected as the case studies to compare and evaluate the precision of FY3F/OMS SO_2 retrievals. One is the area of latitude from 5°S to 5°N and longitude from 30°W to 20°W (Ocean-Area1), and the other is the area of latitude from 5°S to 5°N and longitude from 135°W to 125°W (Ocean-Area2). Due to the geolocation differences between OMS and TROPOMI orbits, the orbital pixels of OMS and TROPOMI DOAS and TROPOMI COBRA SO_2 product over the two clean oceanic regions were resampled to 0.15°×0.15° equal latitude-longitude grid for comparison. As suggested in the TROPOMI README file, only pixels with QA > 0.5 were used for the TROPOMI DOAS SO_2 product. For the cases of clean oceanic regions, TROPOMI COBRA L3 grid PBL SO_2 products were used instead of the COBRA 7km product. For OMS SO_2 retrievals, all pixels with SO_2 column greater than -10 DU are selected for comparison.

For Ocean-Area1, both OMS and TROPOMI show low SO_2 values, and the standard deviations of OMS, TROPOMI DOAS and TROPOMI COBRA SO_2 columns over Ocean-Area1 are 0.2117 DU, 0.2468 DU and 0.1156 DU (resampling to 0.15°×0.15° equal latitude-longitude grid) on August 23, 2024, and 0.2154 DU, 0.4134 DU and 0.1865 DU (resampling to 0.15°×0.15° equal latitude-longitude grid) on November 15, 2024, respectively. For Ocean-Area2, the standard deviations of

OMS, TROPOMI DOAS and TROPOMI COBRA SO_2 columns are 0.2160 DU, 0.2324 DU and 0.1035 DU (resampling to 0.15°×0.15° equal latitude-longitude grid) on August 23, 2024, and 0.2358 DU, 0.3127 DU and 0.1615 DU (resampling to 0.15°×0.15° equal latitude-longitude grid) on November 15, 2024, respectively.

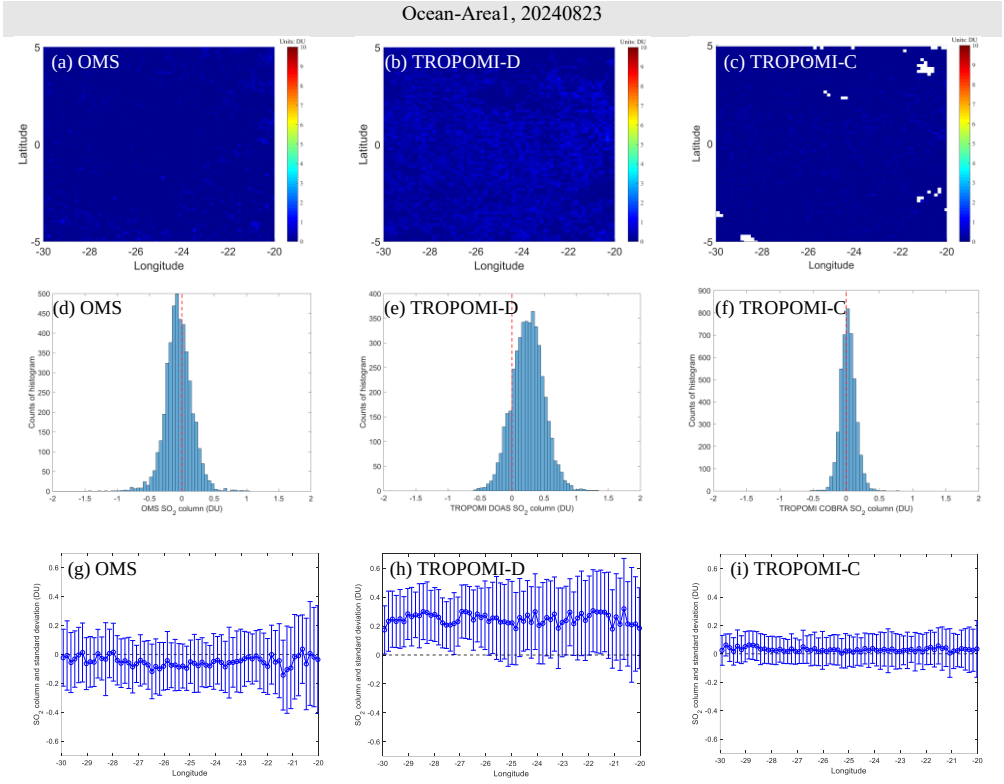

Figure 8: SO_2 retrievals over clean oceanic area (latitude from 5°S to 5°N and longitude from 30°W to 20°W, Ocean-Area1) on August 23, 2024. (a, b, c) Spatial distribution of resampled FY3F/OMS, TROPOMI DOAS (TROPOMI-D) and TROPOMI COBRA (TROPOMI-C) PBL SO_2 columns over Ocean-Area1; (b, d, f) Histogram of resampled OMS, TROPOMI DOAS and TROPOMI COBRA PBL SO_2 columns over Ocean-Area1; (g, h, i) Variation and standard deviations of the latitude-averaged SO_2 columns over Ocean-Area1. Note that OMS pixels with SO_2 column less than -10 and TROPOMI DOAS pixels with QA < 0.5 are assigned the value of -9999. The missing pixels in Figure c are due to quality filtering applied to TROPOMI COBRA data

删除的内容: As shown in Figs. 8, 9, 10, and 11, both the SO_2 values of OMS and TROPOMI over Ocean-Area1 and Ocean-Area2 follow approximately a normal distribution centered around 0, with most values concentrated between -2 DU and 2 DU. However, there are small differences between OMS and TROPOMI SO_2 over clean oceanic regions, which become larger as the pixels approach the edge of the orbit. The differences between OMS and TROPOMI SO_2 columns may be related to differences in local overpass time, observation angles, L1 and L2 processing algorithms. Compared with TROPOMI DOAS SO_2 results, TROPOMI COBRA SO_2 results and OMS DOAS SO_2 results have a lower standard deviation and are closer to zero over Ocean-Area1 and Ocean-Area2. The standard deviation of TROPOMI COBRA SO_2 results over the clean oceanic region is lower than that of OMS DOAS SO_2 results, mainly due to the different retrieval schemes and retrieval fitting windows. As shown in Fig. 4, TROPOMI COBRA uses a fitting window of 310.5–326 nm, where the SO_2 absorption is relatively strong, but the signal tends to be saturated under high volcanic SO_2 concentrations. The comparison results from different dates and different clean oceanic regions show that FY3F/OMS SO_2 retrievals have a reliable precision over low SO_2 emission regions, and the data quality of OMS SO_2 retrievals is relatively stable over time. It is worth noting that the retrieval errors for both OMS and TROPOMI are relatively large at the edges of the orbit. Therefore, the pixels near the edges of the orbit need to be used with caution.

删除的内容: The missing pixels in the Figure c are caused by Nan values in TROPOMI COBRA data.

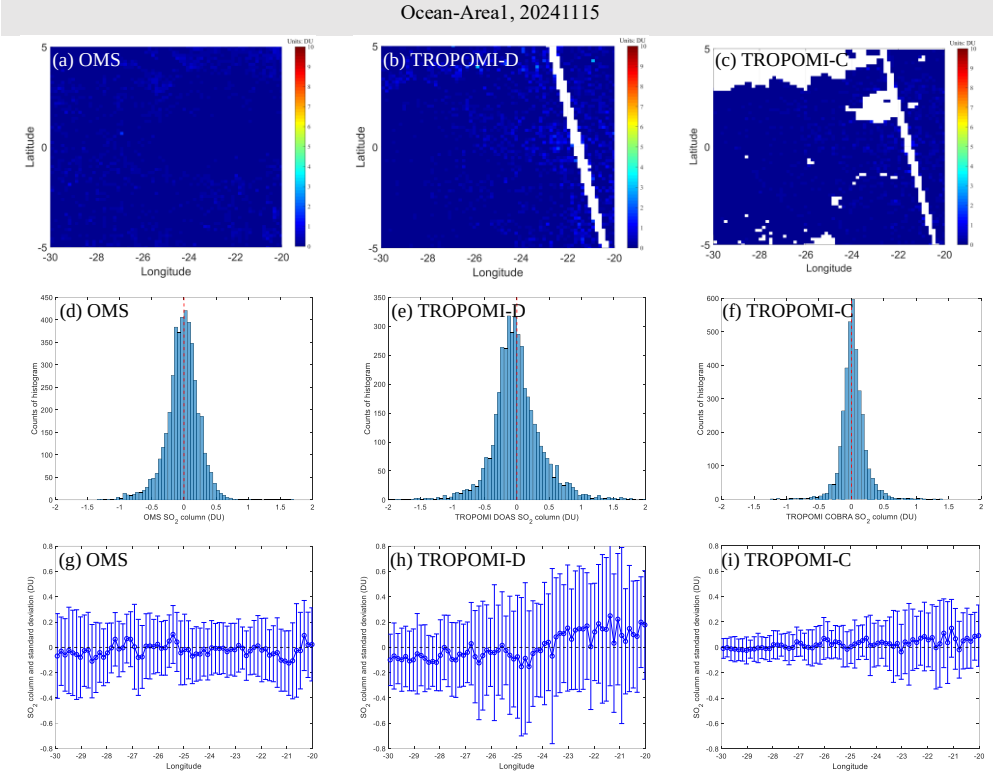

Figure 9: As Fig. 8 but for November 15, 2024. The missing pixels in Figure b are due to the gap between the two TROPOMI orbits, while those in Figure c are due to quality filtering applied to TROPOMI COBRA data.

删除的内容: The missing pixels in the Figures b and c are caused by the gap between the two orbits and the Nan values in TROPOMI COBRA data.

删除的内容: .

As shown in Figs. 8, 9, 10, and 11, both the SO_2 values of OMS and TROPOMI over Ocean-Area1 and Ocean-Area2 follow approximately a normal distribution centered around 0, with most values concentrated between -2 DU and 2 DU. However, there are small differences between OMS and TROPOMI SO_2 over clean oceanic regions, which become larger as the pixels approach the edge of the orbit. The differences between OMS and TROPOMI SO_2 columns may be related to differences in local overpass time, observation angles, L1 and L2 processing algorithms. Compared with TROPOMI DOAS SO_2 results, TROPOMI COBRA SO_2 results and OMS DOAS SO_2 results have a lower standard deviation and are closer to zero over Ocean-Area1 and Ocean-Area2. The standard deviation of TROPOMI COBRA SO_2 results over the clean oceanic region is lower than that of OMS DOAS SO_2 results, mainly due to the different retrieval schemes and retrieval fitting windows. As

shown in Fig. 4, TROPOMI COBRA uses a fitting window of 310.5–326 nm, where the SO_2 absorption is relatively strong, but the signal tends to be saturated under high volcanic SO_2 concentrations.

The comparison of results from different dates and different clean oceanic regions show that FY3F/OMS SO_2 retrievals have a reliable precision over low SO_2 emission regions, and the data quality of OMS SO_2 retrievals is relatively stable over time. It is worth noting that the retrieval errors for both OMS and TROPOMI are relatively large at the edges of the orbit. Therefore, the pixels near the edges of the orbit need to be used with caution.

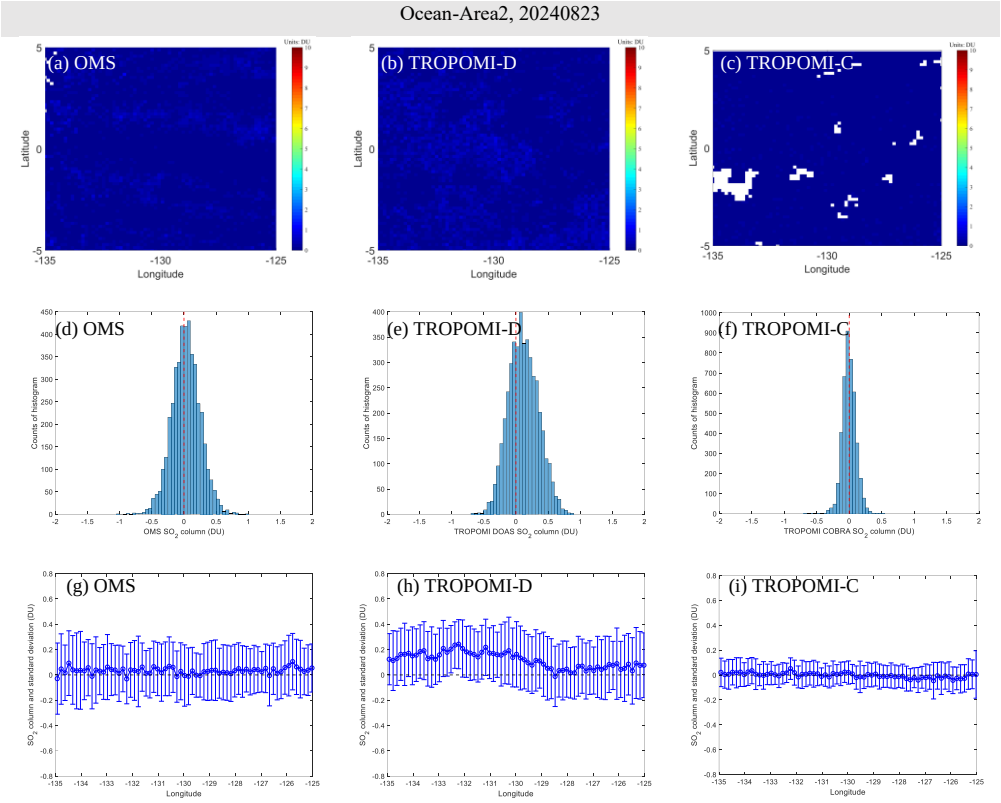

Figure 10: As Fig. 8 but for region Ocean-Area 2 (latitude from 5°S to 5°N and longitude from 135°W to 125°W). The missing pixels in the Figure a are caused by low spatial resolution at the edges of the orbits, and the missing pixels in the Figure c are caused by the quality filtering applied to TROPOMI COBRA data.

删除的内容: Nan values in TROPOMI COBRA data.

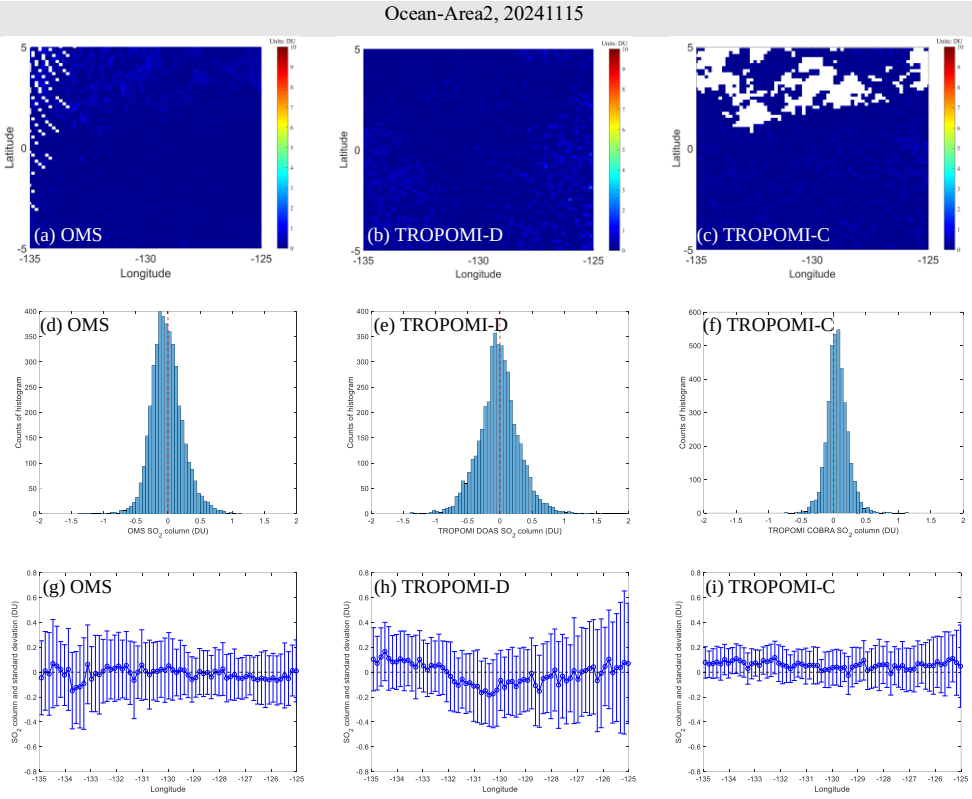

Figure 11: As Fig. 10 but for November 15, 2024. The missing pixels in the Figure a are caused by low spatial resolution at the edges of the orbits, and the missing pixels in the Figure c are caused by the quality filtering applied to TROPOMI COBRA data.

删除的内容: Nan values in TROPOMI COBRA data

4.2 Comparison over volcanic eruptions

The massive amounts of SO_2 released over a short period during volcanic eruptions, as well as their long-distance transport and the subsequent formation of sulfate aerosols, not only influence the global radiative energy balance (Mccormick et al., 1995) but also pose risks to aviation in the tropopause or stratosphere (Miller and Casadevall, 2000). Through the comparison in volcanic regions, the capability of OMS SO_2 retrievals at large columns can be evaluated. In this section, we

took the eruptions of Sundhnúkur volcano and Nyamuragira volcano as case studies for comparing FY3F/OMS SO_2 with TROPOMI DOAS and TROPOMI COBRA 7km SO_2 results. To present the SO_2 maps of OMS and TROPOMI DOAS more clearly, the resampling scheme in section 4.1 was not used in section 4.2. For TROPOMI DOAS, we used all pixels from the TROPOMI DOAS SO_2 product instead of applying QA > 0.5 to filter the high-quality pixels when comparing with the OMS SO_2 results. The reason is that after applying the QA > 0.5 filter, a lot of high SO_2 pixels in TROPOMI DOAS over volcanic regions would be missing, making it difficult to compare with OMS SO_2 results. In this section, TROPOMI COBRA L3 grid 7km SO_2 products were used instead of COBRA PBL products.

The Sundhnúkur volcano is the first case study for comparing FY3F/OMS SO_2 with TROPOMI DOAS and TROPOMI COBRA 7km SO_2 results over a volcanic eruption. On August 22, 2024, Sundhnúkur volcano within the Reykjanes volcanic system began erupting and continued to emit SO_2 for approximately 14 days (https://volcano.si.edu/). The eruption created a fissure approximately 3.9 km long, with lava and smoke reaching a height of about 1 km. The region of latitude from 55 °N to 65 °N and longitude from 30 °W to 5 °W was selected as the study area for the Sundhnúkur volcano. There are two OMS orbits (20240823_1036 and 20240823_1217) (Format: YYYYMMDD_HHMM, UTC time of the first scan line) overpassing the Sundhnúkur volcano region on August 23, 2024. For the OMS orbit 20240823_1217, most of the pixels covering the volcanic region are near the edge of the orbit where the measurement noise tends to be higher. For TROPOMI DOAS, although two orbits (20240823T125304 and 20240823T111134) (Format: YYYYMMDDTHHMMSS, observation start UTC time) passed over the Sundhnúkur volcano area, only orbit 20240823T125304 is presented because most of its pixels over the Sundhnúkur volcano region were near the nadir of the orbit where the data quality is higher. As shown in Fig. 12, both OMS and TROPOMI successfully captured the high SO_2 distribution around the Sundhnúkur volcano on August 23, 2024. The spatial distributions of OMS, TROPOMI DOAS and TROPOMI COBRA SO_2 over Sundhnúkur volcano are similar, but differ at the edge of the SO_2 plume. Compared with OMS orbit 20240823_1036, orbit 20240823_1217 has a local overpass time closer to that of TROPOMI orbit 20240823T125304 in the volcanic region, making the SO_2 results of OMS orbit 20240823_1217 more consistent with those of TROPOMI orbit 20240823T125304. The correlation between OMS and TROPOMI DOAS reaches ~0.87 over the Sundhnúkur volcano on August 23, 2024, while the correlation between OMS and TROPOMI COBRA reaches ~0.76.

However, when SO_2 values exceed 50 DU, OMS SO_2 retrievals are significantly lower than those of TROPOMI DOAS over the Sundhnúkur volcano region on August 23, 2024. Moreover, the relative biases between OMS and TROPOMI DOAS increase with increasing SO_2 columns. This may be attributed to the reason that the OMS SO_2 retrieval uses the 312–326 nm fitting window, where SO_2 has strong absorption and is prone to saturation in the case of high SO_2 concentrations, leading to an underestimation of SO_2 columns. In order to mitigate the risk of saturation, TROPOMI DOAS uses two additional fitting windows (325–335 nm and 360–390 nm) (S5P-BIRA-L2-ATBD-400E) for volcanic eruption cases. In addition, the different overpass time of OMS and TROPOMI, along with varying volcanic eruption strength and meteorological conditions, may also be major contributors to the differences in SO_2 columns of OMS and TROPOMI DOAS. The TROPOMI COBRA SO_2

results retrieved from the 310.5–326 nm window are also lower than those from TROPOMI DOAS, but are more consistent with those from OMS.

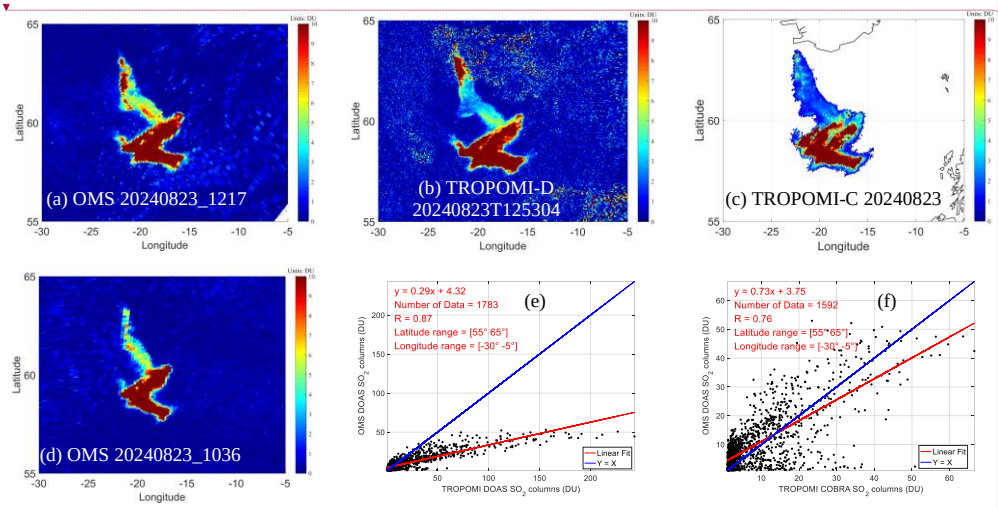

Figure 12: SO_2 retrievals over Sundhnúkur volcano on August 23, 2024. (a, b, c, d) Spatial distribution of FY3F/OMS, TROPOMI DOAS and TROPOMI COBRA 7km SO_2 columns over Sundhnúkur volcano; (e, f) Scatter plots of OMS 20240823_1217 and TROPOMI over Sundhnúkur volcano on August 23, 2024, where pixels with SO_2 columns greater than 1 DU were selected and TROPOMI is resampled to the latitude-longitude grid of OMS. The missing pixels in Figure a are the gap between the two OMS orbits, and the missing pixels in Figure c are due to quality filtering applied to TROPOMI COBRA data.

The Nyamuragira volcano is the second case study for comparing FY3F/OMS SO_2 with TROPOMI DOAS and TROPOMI COBRA 7km SO_2 results over a volcanic eruption. Nyamuragira is Africa's most active volcano and a high-potassium basaltic shield volcano located in the eastern part of the Democratic Republic of the Congo, approximately 25 km north of Lake Kivu and 13 km north-northwest of the Nyiragongo volcano (https://volcano.si.edu/). Based on the Volcanic Explosivity Index (VEI) classification (Newhall and Self, 1982) and eruptive history reports of Nyamuragira from the Global Volcanism Program (GVP), the magnitude of Nyamuragira's eruptions can generally be classified as small to moderate. According to the GVP weekly reports, Nyamuragira had continuing eruptive activities in November 2024. In this section, the region of latitude from 10 °S to 10 °N and longitude from 15 °E to 35 °E was selected as the study area for the Nyamuragira volcano. The spatial distribution maps (Fig. 13) show that OMS, TROPOMI DOAS, and TROPOMI COBRA results clearly detected the high-concentration SO_2 plume from the Nyamuragira eruption, although the shape of the SO_2 plume differs due to differences in overpass time and observation angles. However, as shown in Fig. 14, most of OMS SO_2 retrievals over the Nyamuragira region are higher than the TROPOMI DOAS and TROPOMI COBRA results, which differs from the results for the Sundhnúkur

删除的内容: The Nyamuragira volcano is the second case study for comparing FY3F/OMS SO_2 with TROPOMI DOAS and TROPOMI COBRA 7km SO_2 results over a volcanic eruption. Nyamuragira is Africa's most active volcano and a high-potassium basaltic shield volcano located in the eastern part of the Democratic Republic of the Congo, approximately 25 km north of Lake Kivu and 13 km north-northwest of the Nyiragongo volcano (https://volcano.si.edu/). Based on the Volcanic Explosivity Index (VEI) classification (Newhall and Self, 1982) and eruptive history reports of Nyamuragira from the Global Volcanism Program (GVP), the magnitude of Nyamuragira's eruptions can generally be classified as small to moderate. According to the GVP weekly reports, Nyamuragira had continuing eruptive activities in November 2024. In this section, the region of latitude from 10 °S to 10 °N and longitude from 15 °E to 35 °E was selected as the study area for the Nyamuragira volcano. The spatial distribution maps (Fig. 13) show that OMS, TROPOMI DOAS, and TROPOMI COBRA results clearly detected the high-concentration SO_2 plume from the Nyamuragira eruption, although the shape of the SO_2 plume differs due to differences in overpass time and observation angles. However, as shown in Fig. 14, most of OMS SO_2 retrievals over the Nyamuragira region are higher than the TROPOMI DOAS and TROPOMI COBRA results, which differs from the results for the Sundhnúkur volcano mentioned above. The reason may be attributed to factors such as the different retrieval fitting window and AMF strategies used by OMS SO_2, TROPOMI DOAS and TROPOMI COBRA 7km SO_2. It is worth noting that in Fig. 14, SO_2 column results from OMS and TROPOMI DOAS and TROPOMI COBRA were resampled to 0.15 °×0.15 °equal latitude-longitude grid, and only SO_2 retrievals greater than 1 DU within the Nyamuragira volcano region were selected and summed. For the case of the Nyamuragira volcano, which is located near the equator (unlike the high-latitude Sundhnúkur volcano), it is difficult to find OMS and TROPOMI orbits with close overpass times. As a result of the overpass time differences between OMS and TROPOMI, the plume positions changed between the two measurements making direct comparison difficult.

From the above comparisons between FY3F/OMS SO_2 and TROPOMI DOAS and TROPOMI COBRA 7km SO_2 results, we can see that FY3F/OMS has the capability to monitor volcanic activities, and with high spatial resolution of 7 km ×7 km and a local overpass time different from TROPOMI, FY3F/OMS can contribute to a more effective satellite SO_2 product for the continuous monitoring of global volcanic activity.

删除的内容: the Nan values in TROPOMI COBRA data

带格式的: 正文

volcano mentioned above. The reason may be attributed to factors such as the different retrieval fitting window and AMF strategies used by OMS SO_2, TROPOMI DOAS and TROPOMI COBRA 7km SO_2. It is worth noting that in Fig. 14, SO_2 column results from OMS and TROPOMI DOAS and TROPOMI COBRA were resampled to 0.15°×0.15° equal latitude-longitude grid, and only SO_2 retrievals greater than 1 DU within the Nyamuragira volcano region were selected and summed. For the case of the Nyamuragira volcano, which is located near the equator (unlike the high-latitude Sundhnúkur volcano), it is difficult to find OMS and TROPOMI orbits with close overpass times. As a result of the overpass time differences between OMS and TROPOMI, the plume positions changed between the two measurements making direct comparison difficult.

From the above comparisons between FY3F/OMS SO_2 and TROPOMI DOAS and TROPOMI COBRA 7km SO_2 results, we can see that FY3F/OMS has the capability to monitor volcanic activities, and with high spatial resolution of 7 km×7 km and a local overpass time different from TROPOMI, FY3F/OMS can contribute to a more effective satellite SO_2 product for the continuous monitoring of global volcanic activity.

删除的内容：.

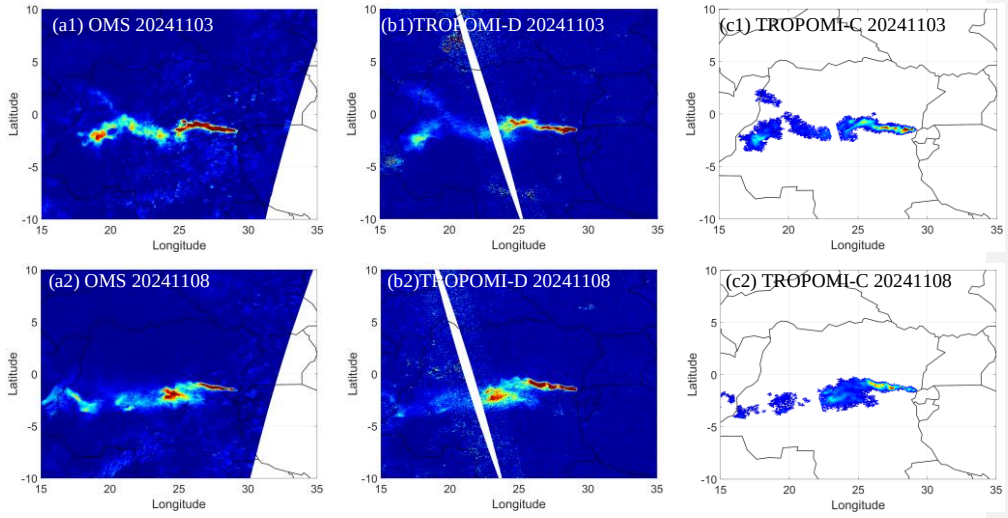

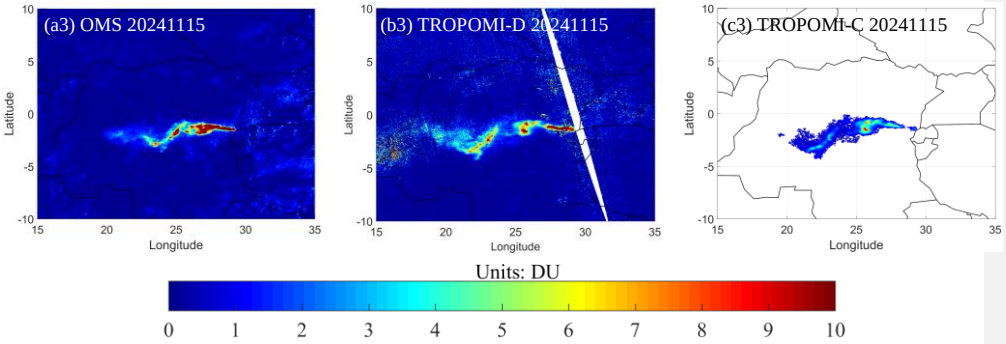

Figure 13: SO_2 retrievals of OMS and TROPOMI over the Nyamuragira volcano on November 3, 8, and 15, 2024. The missing pixels are the gap between the two orbits, or the Nan values in downloaded TROPOMI COBRA data. (a1) OMS SO_2 columns, orbit 20241103_0739; (b1)TROPOMI DOAS SO_2 columns, orbits 20241103T101246 (east) and 20241103T115416 (west); (c1) TROPOMI COBRA 7km L3 SO_2 columns, 20241103; (a2) OMS SO_2 columns, orbit 20241108_0743; (b2)TROPOMI DOAS SO_2 columns, orbits 20241108T101829 (east) and 20241108T115958 (west); (c2) TROPOMI COBRA 7km L3 SO_2 columns, 20241108; (a3) OMS SO_2 columns, orbit 20241115_0709; (b3) TROPOMI DOAS SO_2 columns, orbits 20241115T094602 (east) and 20241115T112732 (west); (c3) TROPOMI COBRA 7km L3 SO_2 columns, 20241115.

带格式的：字体: Times New Roman

删除的内容：.

删除的内容：.

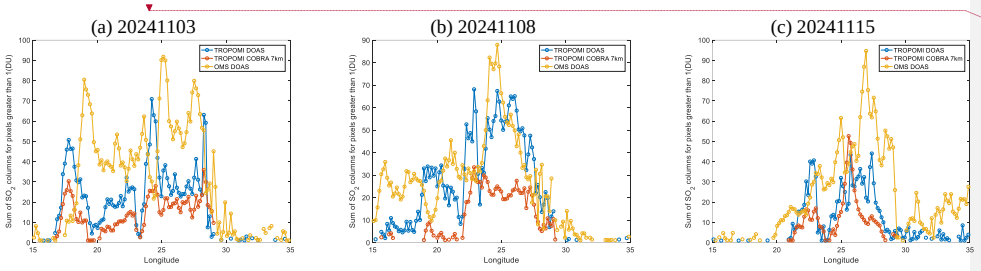

Figure 14: Latitude-summed (latitude from 10 °S to 10 °N) SO_2 columns of OMS, TROPOMI DOAS and TROPOMI COBRA over Nyamuragira volcano on November 3, 8, and 15, 2024. Only pixels with SO_2 columns greater than 1 DU were selected.

4.3 Comparison for anthropogenic emissions

Compared to the monitoring of high SO_2 emissions from natural sources such as volcanoes, the monitoring of anthropogenic SO_2 emissions from satellite observations is more challenging. Firstly, the atmospheric SO_2 from anthropogenic SO_2 emissions is generally much lower compared to that of volcanic eruptions. Secondly, SO_2 from anthropogenic emission is primarily concentrated near the surface. However, the sensitivity of satellite measurements in the UV band near the surface is relatively low because solar UV radiation is partially absorbed and scattered by atmospheric components such as air, aerosols, and clouds during its transmission. As a result, the weakened UV radiation reaching the boundary layer reduces the

sensitivity of satellite instruments to PBL SO_2 and makes it harder to distinguish SO_2 signals from background noise, especially at large solar zenith and satellite viewing angles.

Based on the SO_2 emission sources observed by TROPOMI in 2018 (Fioletov et al., 2020), we selected three representative regions – the Persian Gulf (oil and gas exploration), Norilsk (smelters), and Eastern India (power plants) – to compare three SO_2 column products: OMS SO_2, TROPOMI DOAS SO_2, and TROPOMI COBRA PBL SO_2. These comparisons aim at evaluating the capability of OMS in monitoring SO_2 emissions from anthropogenic sources. Similar to the cases of volcanic eruptions, we used all pixels from the TROPOMI DOAS SO_2 product instead of applying QA > 0.5 to filter the high-quality pixels because the QA > 0.5 filter would remove many high SO_2 pixels over anthropogenic emission regions. In the case of anthropogenic emissions, TROPOMI COBRA L3 grid PBL SO_2 products were used for comparison instead of the COBRA 7km SO_2 products.

The Persian Gulf was selected due to its high anthropogenic emissions, including SO_2 and NO_2, primarily from oil and gas extraction and refining industries (Mardani et al., 2025; Krotkov et al., 2016). This region has a higher probability of clear-sky days and is located in the low-latitude zone, which means relatively high SNR for satellite observations. As shown in Figs. and , OMS effectively detects high SO_2 values over the Persian Gulf while maintaining a lower background noise. Scatter plots from different dates (August 23, 2024, and November 12, 2024) show that (1) The correlation coefficients between OMS and TROPOMI DOAS and TROPOMI COBRA SO_2 remain around 0.5–0.6; (2) TROPOMI COBRA SO_2 retrievals are lower than DOAS results over the Persian Gulf; (3) Additionally, the differences among the three datasets (OMS SO_2, TROPOMI DOAS SO_2, and TROPOMI COBRA PBL SO_2) vary over time: on August 23, 2024, OMS SO_2 retrievals were higher than those from both TROPOMI DOAS and TROPOMI COBRA, whereas on November 12, 2024, OMS SO_2 retrievals were lower than those of TROPOMI DOAS and TROPOMI COBRA. This may be attributed to the factors such as viewing angle, overpass time, local emission variations, and AMF values.

Norilsk in northern Russia within the Arctic Circle is one of the world's biggest sources of anthropogenic SO_2 emissions due to its massive nickel and metal smelting industry (Bauduin et al., 2014). With winter lasting 6 to 9 months and snow covering the ground for most of the year, the region's low temperatures and atmospheric stability hinder pollutant dispersion, leading to persistently high SO_2 concentrations over Norilsk. Large SO_2 emissions cause severe air pollution and acid rain, which make Norilsk one of the most polluted cities in the world. On May 16, 2024, the orbits of OMS and TROPOMI with close local overpass times over Norilsk were selected to reduce the impact of emission and meteorological differences on the comparisons of SO_2 columns. As shown in Fig. 17, both OMS and TROPOMI were able to detect the SO_2 plumes over the Norilsk region. Note that for the OMS SO_2 retrievals over Norilsk on May 16, 2024, the constant AMF=2 was used for the conversion from SCD to VCD. The SO_2 columns from OMS and TROPOMI DOAS have a good correlation of 0.91-0.93 over the Norilsk region. In the case of Norilsk, OMS SO_2 retrievals are slightly lower than those from TROPOMI DOAS, with the average relative biases (|OMS - TROPOMI| / TROPOMI) of the data from the Norilsk region in OMS orbit 20240516_0334 being approximately 22% (excluding outliers with relative biases greater than 200% and SO_2 columns smaller than 1 DU), and for OMS orbit 20240516_0516 being approximately 18% (applying the same filtering criteria). The

域代码已更改

域代码已更改

删除的内容:

TROPOMI COBRA PBL L3 products which have mostly Nan values over the Norilsk region are not presented in this section.

India's SO_2 emissions are mainly from coal fired power plants, transportation, and agricultural activities, which are growing rapidly, increasing by more than 100% from 2005 to 2015 (Krotkov et al., 2016; Kuttippurath et al., 2022). As shown in Fig. 18, OMS also successfully captured the high SO_2 plumes in Eastern India, but most of OMS SO_2 retrievals are lower than those from TROPOMI DOAS. This is mainly attributed to the simplified strategy of OMS using a constant AMF=1 for the Indian region. Future work will consider using Indian local SO_2 profiles to calculate specific AMFs over India in order to improve the accuracy of OMS SO_2 retrievals over this area. It is worth noting that the ranges of the color bars in Figs. 18a1-a3 are different from others to more clearly present the OMS SO_2 retrievals over Eastern India. Figure 18 also shows that due to different local overpass times, when the SO_2 pollution area in India is located at the edge of the TROPOMI orbit where large retrieval errors often occur, OMS can provide effective data support to fill the monitoring gaps caused by TROPOMI's edge-related pixels. These comparisons demonstrate that OMS can distinguish the effective daily SO_2 information from background noises.

带格式的: 字体: 10 磅, 非加粗

删除的内容: Figure 18

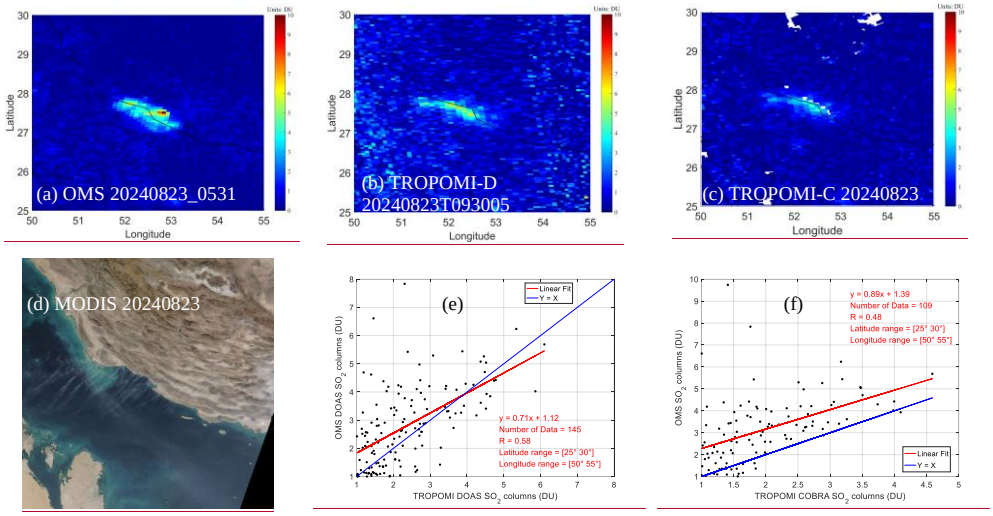

Figure 15: SO_2 retrievals over the Persian Gulf on August 23, 2024. (a, b, c) Spatial distribution of FY3F/OMS, TROPOMI DOAS and TROPOMI COBRA PBL SO_2 columns over Persian Gulf; (d) True Color Image of the Persian Gulf from Terra/MODIS (Source: https://worldview.earthdata.nasa.gov/); (e, f) Scatter plots of FY3F/OMS, TROPOMI DOAS and TROPOMI COBRA PBL SO_2 over the Persian Gulf on August 23, 2024, where pixels with SO_2 columns greater than 1 DU were selected and TROPOMI is resampled to the latitude-longitude grid of OMS. Note that the missing pixels in Figure c are due to quality filtering applied to TROPOMI COBRA data.

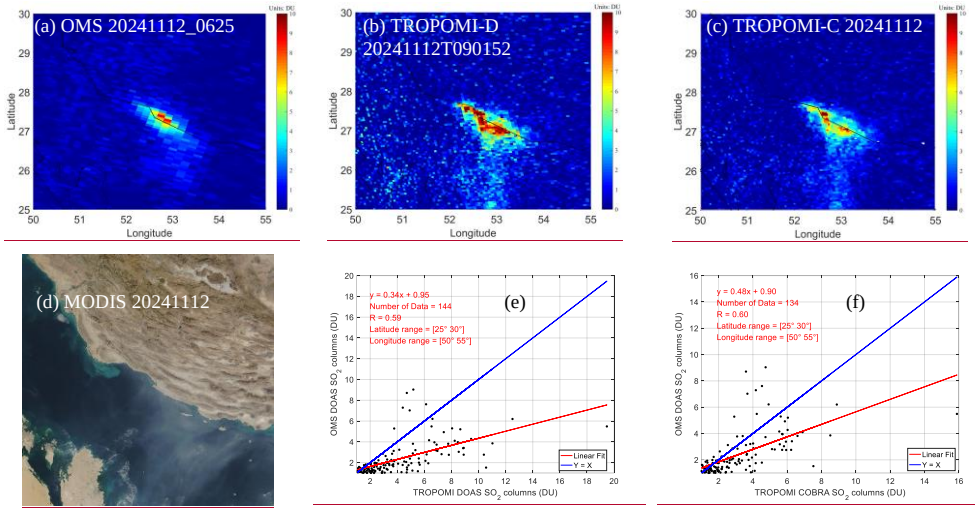

Figure 16: As Fig. but for November 12, 2024.

域代码已更改

删除的内容：

Norilsk in northern Russia within the Arctic Circle is one of the world's biggest sources of anthropogenic SO_2 emissions due to its massive nickel and metal smelting industry (Bauduin et al., 2014). With winter lasting 6 to 9 months and snow covering the ground for most of the year, the region's low temperatures and atmospheric stability hinder pollutant dispersion, leading to persistently high SO_2 concentrations over Norilsk. Large SO_2 emissions cause severe air pollution and acid rain, which make Norilsk one of the most polluted cities in the world. On May 16, 2024, the orbits of OMS and TROPOMI with close local overpass times over Norilsk were selected to reduce the impact of emission and meteorological differences on the comparisons of SO_2 columns. As shown in Fig. 17, both OMS and TROPOMI were able to detect the SO_2 plumes over the Norilsk region. Note that for the OMS SO_2 retrievals over Norilsk on May 16, 2024, the constant AMF=2 was used for the conversion from SCD to VCD. The SO_2 columns from OMS and TROPOMI DOAS have a good correlation of 0.91-0.93 over the Norilsk region. In the case of Norilsk, OMS SO_2 retrievals are slightly lower than those from TROPOMI DOAS, with the average relative biases (|OMS - TROPOMI| / TROPOMI) of the data from the Norilsk region in OMS orbit 20240516_0334 being approximately 22% (excluding outliers with relative biases greater than 200% and SO_2 columns smaller than 1 DU), and for OMS orbit 20240516_0516 being approximately 18% (applying the same filtering criteria). The TROPOMI COBRA PBL L3 products which have mostly Nan values over the Norilsk region are not presented in this section.

India's SO_2 emissions are mainly from coal fired power plants, transportation, and agricultural activities, which are growing rapidly, increasing by more than 100% from 2005 to 2015 (Krotkov et al., 2016; Kuttippurath et al., 2022). As shown in Fig. 18, OMS also successfully captured the high SO_2 plumes in Eastern India, but most of OMS SO_2 retrievals are lower than those from TROPOMI DOAS. This is mainly attributed to the simplified strategy of OMS using a constant AMF=1 for the Indian region. Future work will consider using Indian local SO_2 profiles to calculate specific AMFs over India in order to improve the accuracy of OMS SO_2 retrievals over this area. It is worth noting that the ranges of the color bars in Figs. 18a1-a3 are different from others to more clearly present the OMS SO_2 retrievals over Eastern India. Figure 18 also shows that due to different local overpass times, when the SO_2 pollution area in India is located at the edge of the TROPOMI orbit where large retrieval errors often occur, OMS can provide effective data support to fill the monitoring gaps caused by TROPOMI's edge-related pixels. These comparisons demonstrate that OMS can distinguish the effective daily SO_2 information from background noises.

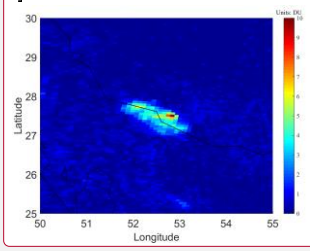

...

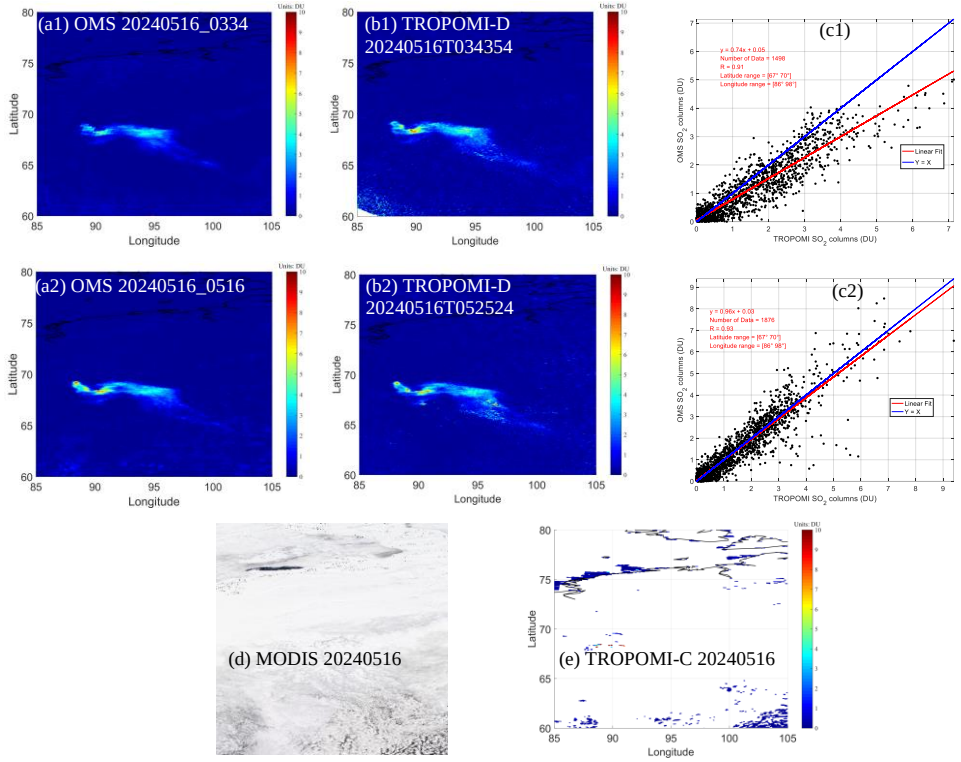

Figure 17: SO_2 retrievals over Norilsk on May 16, 2024. (a1-2, b1-2) Spatial distribution of FY3F/OMS and TROPOMI DOAS SO_2 columns over Norilsk; (c1-2) Scatter plots of OMS and TROPOMI DOAS SO_2 columns over Norilsk on May 16, 2024, where pixels with SO_2 columns greater than 1 DU were selected and TROPOMI is resampled to the latitude-longitude grid of OMS; (d)True Color Image of Norilsk from Terra/MODIS on May 16, 2024; (e) SO_2 columns from TROPOMI COBRA PBL over Norilsk on May 16, 2024. Note that the missing pixels in Figure e are due to quality filtering applied to TROPOMI COBRA data.

删除的内容: **Nan values in TROPOMI COBRA data**

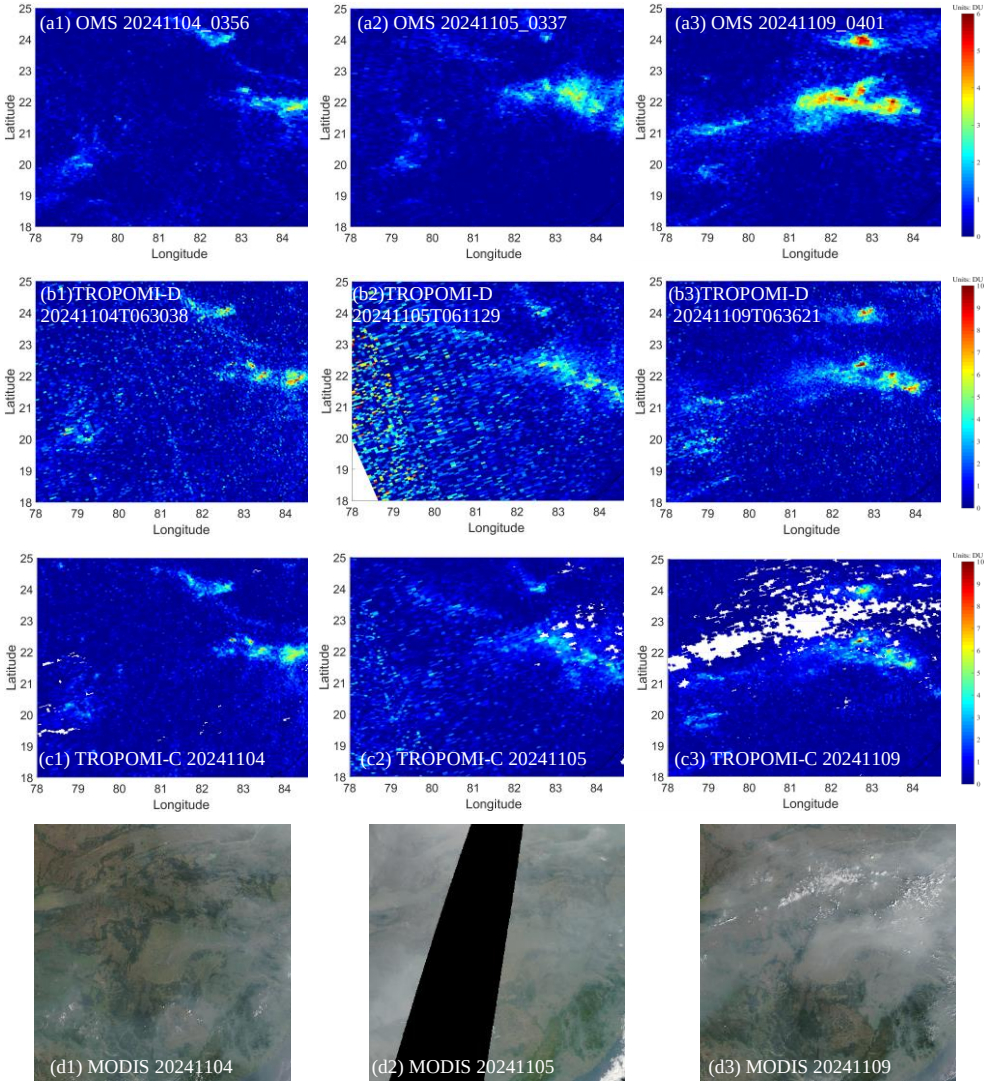

Figure 18: SO_2 retrievals over Eastern India on November 4, 5, and 9, 2024. (a1-3, b1-3, c1-3) Spatial distribution of FY3F/OMS, TROPOMI DOAS and TROPOMI COBRA PBL SO_2 columns over Eastern India; (d1-d3) True Color Image of Eastern India

from Terra/MODIS on November 4, 5, and 9, 2024. The missing pixels in the Figures c1-c3 are caused by the quality filtering applied to TROPOMI COBRA data.

删除的内容: Nan values in TROPOMI COBRA data

5 Error analysis

The main error sources in the OMS DOAS SO_2 retrieval include instrument-related errors, DOAS SCD spectral fitting errors, AMF uncertainties, and the residual error after background offset correction. Instrument-related errors include spectral and radiometric calibration errors, degradation of the instrument, stray light contamination and non-uniformity of the diffuser plate, which introduce systematic biases in both radiance and irradiance measurements. DOAS SCD spectral fitting errors include uncertainties in the absorption cross-sections of SO_2 and O_3, interference from strong O_3 absorption, the Ring effect caused by inelastic scattering, and the selection of the polynomial order in spectral fitting which may introduce biases if not appropriately chosen. The AMF, which is crucial for the accuracy of SO_2 retrieval, is affected by the uncertainties in SO_2 vertical profile, surface reflectance, clouds and aerosols, and surface height. Moreover, the background offset correction may introduce additional uncertainties, especially in high SO_2 areas.

Considering these error sources and assuming that they are independent of each other, the total uncertainty in the retrieved SO_2 column can be approximated as:

$$\sigma_{SO_2} = \sqrt{\left(\frac{\sigma_{\mathrm{SCD}}}{\mathrm{AMF}}\right)^2 + \left(\frac{\sigma_{\mathrm{SCD}}^{\mathrm{back}}}{\mathrm{AMF}}\right)^2 + \left(\frac{(\mathrm{SCD}-\mathrm{SCD}^{\mathrm{back}})\cdot\sigma_{\mathrm{AMF}}}{\mathrm{AMF}^2}\right)^2} \quad \text{(Eq. 3)}$$

删除的内容: 2

where σ_{SCD} is the random error from DOAS SO_2 SCD spectral fitting including instrument-related noise, $\sigma_{\mathrm{SCD}}^{\mathrm{back}}$ is the residual systematic error after background offset correction, and σ_{AMF} is the AMF uncertainty which includes two components: one is related to the atmospheric scattering weight and the other one is associated with the SO_2 profile shape.

5.1 Errors in SCD retrieval

The errors in OMS irradiance and radiance measurements are one of the main error sources of SO_2 SCD retrievals. These errors significantly affect the accuracy of OMS SO_2 retrievals, and are the main causes of the systematic overestimation or underestimation of SO_2 retrievals, such as along-track stripes at specific viewing angles and cross-track asymmetry in SO_2 SCD retrievals (Boersma et al., 2004). The OMS irradiance and radiance uncertainties mainly depend on viewing angle, wavelength, and optical degradation. The viewing angle dependence, caused by calibration inaccuracies, results in unequal responses for all viewing angles (one viewing angle corresponds to one cross-track position). With increasing optical degradation and inaccurate spectral calibration, more errors can be introduced into the irradiance and radiance spectra. This degradation is difficult to monitor and calibrate, because no accurate standards over the full OMS wavelength range are readily available. Meanwhile, these errors in solar irradiance and earth radiance are not constant and can change with time and location, making it difficult to correct their impact on SO_2 retrievals. After one year in orbit, the intensity of OMS irradiance at the shorter wavelength of 317 nm has decreased by about 8.83%, while at the longer wavelength of 331 nm, it

删除的内容: be monitored and calibrated

has decreased by about 6.07%. Using the TSIS HSRS hybrid solar reference spectrum instead of the OMS irradiance measurements can mitigate the impact of viewing angle dependence and degradation on OMS SO_2 retrieval. However, since the solar reference spectrum does not contain the instrument characteristics, it may introduce systematic overestimation or underestimation in SO_2 column retrievals. These systematic biases caused by the TSIS HSRS can be partially reduced through background offset correction but cannot be fully eliminated.

The temperature dependence and uncertainties of absorption cross-section spectra can affect the accuracy of DOAS SCD spectral fitting. The OMS SO_2 SCD retrieval utilizes the Bogumil SO_2 and O_3 absorption cross-section spectra at 273 K and 223 K for DOAS SCD fitting (Bogumil et al., 2003). However, the SO_2 and O_3 absorption cross-sections exhibit strong temperature dependence, which affects the accuracy of retrieved SO_2 SCDs when using the constant 273 K SO_2 and 223 K O_3 absorption cross-sections. The SO_2 SCD retrievals increase accordingly as higher-temperature absorption cross-sections are used (Yan et al., 2014). The differences in SCD retrievals caused by temperature-dependent absorption cross-sections increase with increasing SO_2 columns. For example, compared to SCD retrievals using the 203K absorption cross-sections, the differences in SO_2 SCDs can reach a maximum of ~25 DU (with SCDs around 60 DU) (Yan et al., 2014). In addition to the temperature dependence, the uncertainty of the SO_2 and O_3 absorption cross-sections is also one of the error sources in the SO_2 SCD retrievals. Systematic errors in slant columns due to SO_2 cross-section uncertainties are estimated to be around 6% in the 312–326 nm fitting window (Vandaele et al., 2009). The uncertainty of the SO_2 absorption cross-sections from Bogumil et al. (2003) varies with temperature, being 2.8% at 293 K and 3.0% at lower temperatures. The uncertainty of O_3 absorption cross-sections from Bogumil et al. (2003) is approximately 3.1% or less. Therefore, to improve the accuracy of OMS SO_2 retrievals, it is essential to account for the variations in the SO_2 absorption cross-section with temperature and altitude, especially in cases of volcanic eruptions. Future work will incorporate accurate and real-time temperature and SO_2 profile data to account for temperature-dependent effects in OMS SO_2 retrievals.

In the UV wavelength band, the Ring effect is a non-negligible part of the DOAS SCD fitting process. As shown in Fig. 19, the Ring spectrum convolved with the OMS ISRF varies with SZA, VZA, O_3 column and AS within the 310–330 nm wavelength range. The variation of the Ring spectrum with RAA is negligible and is therefore not presented. The mean percentage change in the Ring spectrum is approximately 27.67% (absolute deviation: 0.0025) as the O_3 column varies from 175 DU to 575 DU, 47.34% (absolute deviation: 0.0048) as the AS varies from 0 to 1, 24.18% (absolute deviation: 0.0021) as the VZA varies from 0 ° to 75 °, and 45.29% (absolute deviation: 0.0047) as the SZA varies from 0 ° to 80 °. However, in this study, a single Ring spectrum simulated with the SCIATRAN model was used to retrieve OMS SO_2 for all pixels. The reason is that although the Ring spectrum varies significantly with SZA, VZA, O_3 column, and AS within the 310–330 nm wavelength range, the impact of Ring spectrum variability on SO_2 retrievals is relatively small due to the weak correlation between the Ring spectrum and the satellite TOA reflectance, especially in the case of volcanic eruptions with high SO_2 concentrations. Moreover, using Ring spectra that vary with SZA, VZA, O_3 column, and AS within the 310–330 nm wavelength range require constructing a large lookup table, which would significantly increase computational cost for OMS SO_2 column retrievals.

已下移 [1]: In this study, one single Ring spectrum simulated with the SCIATRAN model was used to retrieve OMS SO_2 for all pixels.

删除的内容: in this study

已移动(插入) [1]

删除的内容: I

删除的内容: one

删除的内容: A

删除的内容: its impact

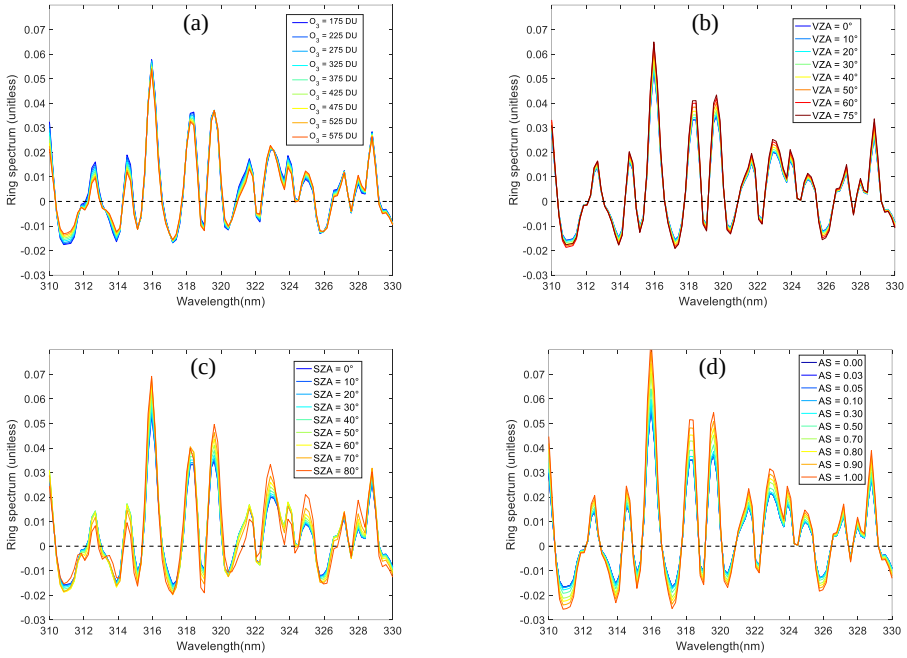

Figure 19: Variation of Ring spectrum with O_3, VZA, SZA and surface reflectivity (AS). Ring spectrum was calculated with the SCIATRAN model, convolved with the OMS ISRF. The default SCIATRAN settings for the Ring spectrum are as follows: wavelength step=0.2 nm, clear sky, HS=0 km, O_3=275 DU, AS=0.05, SZA=30 °, VZA=0 °, RAA=0 °.

Additionally, the accuracy of DOAS SCD fitting is also influenced by the following factors: (1) Interference from strong O_3 absorption in the retrieval fitting window. Due to the overlap of O_3 and SO_2 absorption in the UV wavelength and the fact that the atmospheric O_3 absorption is often much higher than that of SO_2, the UV radiation reaching the near-surface (the primary altitude of anthropogenic SO_2 emissions) is weakened, resulting in a lower SNR. When using the weakened radiance and DOAS fitting to simultaneously retrieve O_3 and SO_2, the strong O_3 absorption signal may overshadow the SO_2 absorption information, leading to errors in the DOAS SO_2 SCD retrievals. Sensitivity analysis shows that a 1% increase in O_3 can lead to approximately a 5% decrease in DOAS SO_2 retrievals (Yan et al., 2017). (2) Selection of retrieval fitting window. Different retrieval fitting windows have varying SO_2 absorption features, O_3 absorption interference, and SNR. The scheme using a single retrieval fitting window of 312–326 nm for OMS SO_2 SCD retrieval may lead to the underestimation of SO_2 columns in the cases of volcanic eruptions or high-reflectivity surfaces. However, employing multiple fitting

删除的内容： for high SO_2 concentrations due to the weak correlation between the Ring spectrum and the satellite TOA reflectance. However, for low SO_2 concentrations, the influence is non-negligible. .
Additionally, the accuracy of DOAS SCD fitting is also influenced by the following factors: (1) Interference from strong O_3 absorption in the retrieval fitting window. Due to the overlap of O_3 and SO_2 absorption in the UV wavelength and the fact that the atmospheric O_3 absorption is often much higher than that of SO_2, the UV radiation reaching the near-surface (the primary altitude of anthropogenic SO_2 emissions) is weakened, resulting in a lower SNR. When using the weakened radiance and DOAS fitting to simultaneously retrieve O_3 and SO_2, the strong O_3 absorption signal may overshadow the SO_2 absorption information, leading to errors in the DOAS SO_2 SCD retrievals. Sensitivity analysis shows that a 1% increase in O_3 can lead to approximately a 5% decrease in DOAS SO_2 retrievals (Yan et al., 2017). (2) Selection of retrieval fitting window. Different retrieval fitting windows have varying SO_2 absorption features, O_3 absorption interference, and SNR. The scheme using a single retrieval fitting window of 312–326 nm for OMS SO_2 SCD retrieval may lead to the underestimation of SO_2 columns in the cases of volcanic eruptions or high-reflectivity surfaces. However, employing multiple fitting windows may lead to inconsistencies among results from different retrieval fitting windows. (3) Low-order polynomial. In DOAS retrievals, low-order polynomials are used to remove slow-varying components, such as aerosol scattering and broad spectral features of absorption. If the polynomial order is too low, it may fail to effectively remove slow-varying components, while if it is too high, overfitting may occur, leading to partial removal of the true SO_2 signal. These errors in SCD propagate into the final OMS SO_2 VCD results, degrading the accuracy and applicability of the OMS SO_2 product. .

带格式的： 正文

windows may lead to inconsistencies among results from different retrieval fitting windows. (3) Low-order polynomial. In DOAS retrievals, low-order polynomials are used to remove slow-varying components, such as aerosol scattering and broad spectral features of absorption. If the polynomial order is too low, it may fail to effectively remove slow-varying components, while if it is too high, overfitting may occur, leading to partial removal of the true SO_2 signal. These errors in SCD propagate into the final OMS SO_2 VCD results, degrading the accuracy and applicability of the OMS SO_2 product.

5.2 Errors from AMF

The AMF is also one of the primary error sources of OMS SO_2 VCD retrieval. It can be calculated by using Box-AMF from forward radiative transfer model and local SO_2 profile (Chen et al., 2009; Wagner et al., 2007; Palmer et al., 2001; Boersma et al., 2004). In this study, due to the difficulty in obtaining accurate and satellite-synchronized global SO_2 profiles, two AMF constants under typical conditions were used to convert the OMS SO_2 SCD to VCD (see section 3.5 for more information).

However, due to the heterogeneity of the global land cover and the variability of atmospheric conditions and SO_2 emission sources, the approximation using constant AMFs can introduce large uncertainties into the final SO_2 VCD retrieval. The AMF value is influenced by multiple factors including wavelength, SZA, VZA, RAA, AS, HS (also referred to as terrain height), O_3 column, SO_2 vertical profile shape, and cloud fraction and altitude (Lee et al., 2009). To analyze the impact of these factors on AMF calculation, we used the SCIATRAN as forward radiative transfer model (Rozanov et al., 2005) to compute Box-AMF under different forward model settings. Box-AMFs corresponding to each set of forward input settings are stored as a function of altitude, representing the atmospheric contribution from each layer.

Figure 20 illustrates the variation of SCIATRAN Box-AMF with SZA, VZA, RAA, AS, HS, wavelength, and O_3 column. The forward model settings remain consistent across all cases, except for the variable being analyzed: SZA = 32.9 °, VZA = 0 °, RAA = 0 °, LER AS = 0.05, HS = 0 km, wavelength = 320 nm, O_3 column = 365 DU, clear sky, and with the assumption of surface reflectance as LER. As shown in Figs. 20a-b, at lower altitudes, Box-AMF is relatively insensitive to changes in SZA and VZA within the range of 0–50 °. However, at higher altitudes (e.g., above 5km), the Box-AMF generally increases with increasing SZA and VZA due to the longer atmospheric path length at larger angles, which enhances the contribution of each atmospheric layer to the total AMF. Note that when SZA or VZA is greater than 73.5 °, the Box-AMF has a significant decrease below altitude 10 km compared to the values at other angles. As shown in Fig. 20c, the variation of Box-AMF with RAA is negligible. Box-AMF increases as surface reflectance increases (Fig. 20d) due to higher reflectivity enhancing atmospheric multiple scattering, which increases the photon path length and thereby raises Box-AMF values. When LER surface reflectance changes from 0 to 1, the surface Box-AMF increases from 0.23 to 4.14, an increase of approximately 1700%. However, the increase of surface reflectance also changes the vertical shape of Box-AMF, shifting it from increasing with altitude to decreasing with altitude. Fig. 20e shows that the Box-AMF decreases with increasing terrain height, as higher surface elevation reduces the atmospheric column above the ground, leading to less scattering and decreased sensitivity. The variation of Box-AMF with wavelength ranging from 310 nm to 330 nm (Fig. 20f) shows that Box-AMF

删除的内容: It is typically computed as the weighted average of altitude-dependent Box-AMFs (equivalent to scattering weights) across all layers, with the weights determined by the SO_2 distribution in each layer (Eq. 3) (Chen et al., 2009; Wagner et al., 2007; Palmer et al., 2001; Boersma et al., 2004):

$$AMF = \sum_i \text{Box-AMF}_i \times \frac{c_i \cdot \Delta h_i}{\sum_j c_j \cdot \Delta h_j} \quad \text{(Eq. 3)}$$

Where c_i represents the SO_2 number density in the i-th layer, and Δh_i denotes the thickness of that layer.
Box-AMFs quantify the contribution of each atmospheric layer to the total AMF and allows for flexible updates of AMF with new SO_2 profiles, eliminating the procedure of rebuilding the AMF lookup table.

带格式的: 字体: 10 磅, 非加粗

删除的内容: Figure 20Figure 20

带格式的: 字体: 10 磅, 非加粗

increases with increasing wavelength. The difference in Box-AMF at different wavelengths varies with altitude. For example, near the surface, when the wavelength increases from 310 nm to 330 nm, the surface Box-AMF increases from 0.28 to 0.48, a rise of 71.13%; At an altitude of 10 km, the Box-AMF increases from 1.69 to 2.36, a rise of 39.57%. Note that for most cases in this study, the wavelength 320 nm, which is approximately at the center of the SO_2 retrieval window (312-326 nm), was chosen to perform the SCIATRAN Box-AMF calculation. The variation of Box-AMF with the O_3 column from 125 DU to 575 DU (Fig. 20g) shows that, compared to other influencing factors, O_3 column has a relatively weak impact on Box-AMF, especially for altitudes below 5 km. The Box-AMF gradually decreases as the O_3 column increases. The differences in Box-AMF under different O_3 column conditions are more noticeable between altitudes of 5 km and 25 km. For example, at an altitude of 15 km, Box-AMF decreases from 2.41 to 2.07 as the O_3 column increases from 125 DU to 575 DU, a decrease of about 14%.

As seen from the above results, compared to other influencing factors, surface reflectance has a relatively strong impact on Box-AMF, thus affecting the accuracy of AMF calculations, especially in anthropogenic emission regions where SO_2 is concentrated near the surface. The errors of Box-AMF from surface reflectance primarily come from two aspects. One is the errors in the surface reflectance climatology. In many satellite products, for each pixel, a surface reflectance climatology (such as from OMI (Kleipool et al., 2008) or TROPOMI (Tilstra et al., 2024)) is interpolated to obtain the corresponding surface reflectance, which is then used as input to calculate the corresponding Box-AMF. The uncertainties in the surface reflectance climatology and interpolation errors due to the spatial resolution differences between the satellite observations and surface reflectance climatology can degrade the accuracy of the Box-AMF calculations. The sensitivity analysis of AS error on SCIATRAN Box-AMF (Fig. 21), which was conducted by introducing a 1% and 0.01 perturbation in AS values ranging from 0.01 to 0.90, shows that (1) The uncertainties in Box-AMF due to a 1% and 0.01 AS variation show a decreasing trend with increasing altitude, meaning that Box-AMF is more sensitive to AS at lower altitudes. (2) The uncertainties of Box-AMF due to a 1% AS variation increase as the AS increases, while those due to a 0.01 AS variation decrease as the AS increases. When AS is small (e.g., AS = 0.01, 0.03, 0.05), a 1% variation in AS can lead to less than a 0.5% change in Box-AMF near the surface. However, when AS ranges from 0.8 to 0.9, the uncertainties of Box-AMF due to a 1% AS variation can reach up to 1.1%-1.2% near the surface. Another aspect affecting the accuracy of Box-AMF due to surface reflectance is the assumption of surface reflectance as LER during SCIATRAN Box-AMF calculation. Surface reflectivity, which depends on the surface properties and the geometry of incident and reflected light, is not uniformly distributed in all directions (i.e., anisotropy). This anisotropy is typically described by the bidirectional reflectance distribution function (BRDF). However, due to more scattering in the UV, this effect is more relevant at longer wavelengths. Therefore, accurate AS input is crucial for the accuracy of Box-AMF calculation, especially in regions with high surface reflectance.

Neglecting forward model errors, Figure 22 shows the dependence of AMF on SZA, VZA, AS, wavelength, O_3 column, and SO_2 profiles. The AMFs were calculated with SCIATRAN Box-AMFs using six assumed SO_2 profiles. Here six SO_2 profiles were constructed, representing clean conditions, low, medium, and high anthropogenic SO_2 emissions, volcanic degassing with plume heights around 2 km, and volcanic eruptions with plume heights around 6 km. As shown in Fig. 22, although

删除的内容：.

删除的内容: As shown in Eq. 3, the shape of the SO_2 vertical profile is important for the calculation of AMF. Since the actual vertical distribution of atmospheric SO_2 is often difficult to get, a priori profiles from models are commonly used in AMF calculations. For regions with anthropogenic emissions, atmospheric chemistry models like GEOS-Chem and TM5 are often used to provide global SO_2 profiles for AMF calculation. The uncertainties in the SO_2 vertical profile can introduce errors into AMF calculations. In future work, we aim to incorporate high-resolution and satellite-synchronized SO_2 vertical profiles to improve the accuracy of AMF.

带格式的: 字体: 10 磅, 非加粗, 检查拼写和语法

带格式的: 下标

AMF values are generally close to 1 under typical atmospheric and surface conditions (non-ice/snow-covered), the magnitude of biases introduced by the simplified AMF approach (AMF=1 for clean regions and non-ice/snow-covered areas, while the other is AMF=2 for the ice/snow-covered areas) varies significantly with different conditions. Surface albedo is the major factor affecting AMF accuracy. For instance, AMFs can differ by up to a factor of three between AS = 0.05 and AS = 0.8. Furthermore, as shown in Eq. 2 and Fig. 22, the shape of the SO_2 vertical profile is critical for accurate AMF calculation. In extreme scenarios, such as volcanic eruptions with plume altitudes around 6 km and SO_2 columns of 120 DU, the use of a simplified AMF may lead to an overestimation of total SO_2 by a factor of 1.5–2. Since the actual vertical distribution of atmospheric SO_2 is often difficult to get, a priori profiles from models are commonly used in AMF calculations. For regions with anthropogenic emissions, atmospheric chemistry models like GEOS-Chem and TM5 are often used to provide global SO_2 profiles for AMF calculation. The uncertainties in these profiles can also propagate into AMF calculations. In future work, we aim to incorporate high-resolution and satellite-synchronized SO_2 vertical profiles to improve the accuracy of AMF.

Additionally, for SO_2 retrievals from high spatial resolution satellite observations, it is often necessary to build a Box-AMF lookup table (LUT) by using radiative transfer model that considers variables such as SZA, VZA, RAA, AS, HS, wavelength, O_3 column, and cloud cover. The corresponding Box-AMF values for each satellite observation pixel are then obtained through interpolation within the LUT. This approach significantly improves the efficiency of retrieval, avoiding excessive computational time that would result from repeatedly running the radiative transfer model. However, the LUT approach may introduce new errors into the Box-AMF results. First, LUT are typically constructed based on specific atmospheric conditions and forward input parameters, which may not accurately represent real atmospheric conditions. Secondly, the interpolation process within the LUT introduces further uncertainties into the Box-AMF results.

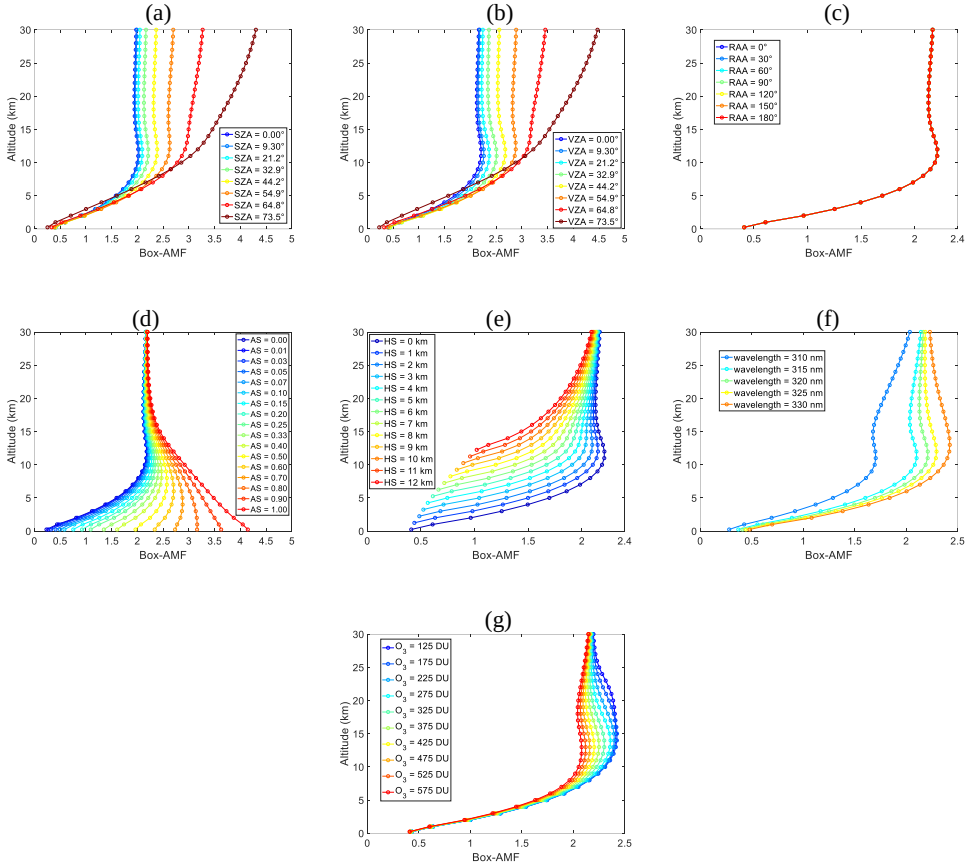

Figure 20: Variation of Box-AMF with SZA, VZA, RAA, AS, HS, wavelength, and O_3 column. The default SCIATRAN settings for Box-AMF calculation are as follows: wavelength=320 nm, clear sky, HS=0 km, O_3=275 DU, AS=0.05, SZA=32.9°, VZA=0°, RAA=0°.

删除的内容: 2020

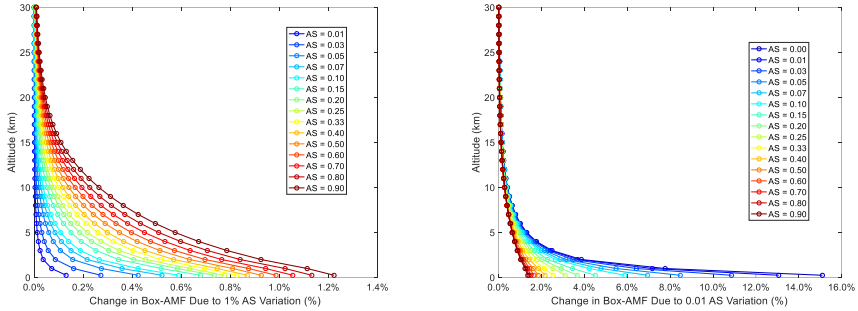

Figure 21: Sensitivity analysis of AS error on SCIATRAN Box-AMF calculation, which was conducted by introducing a 1% (left) and 0.01 (right) perturbation in AS values ranging from 0.01 to 0.90. The other default SCIATRAN settings for Box-AMF calculation are as follows: wavelength=320 nm, clear sky, HS=0 km, O_3=275 DU, SZA=32.9 °, VZA=0 °, RAA=0 °.

删除的内容: 2121

删除的内容: Sensitivity analysis of AS error on SCIATRAN Box-AMF calculation.

带格式的: 正文

(a) (b)

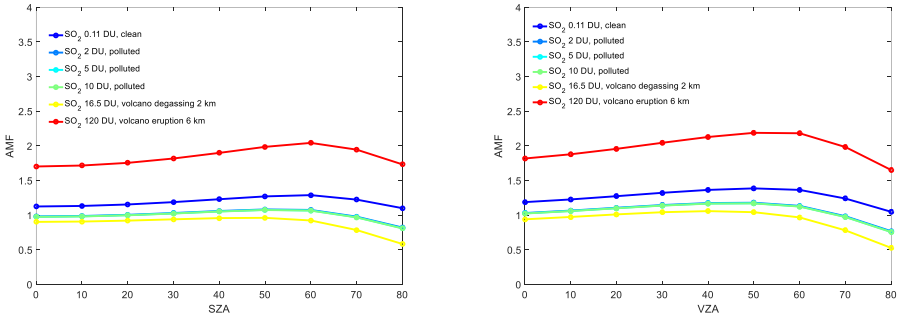

带格式的: 字体: (中文) +中文正文 (宋体), (中文) 中文(中国)

(c)

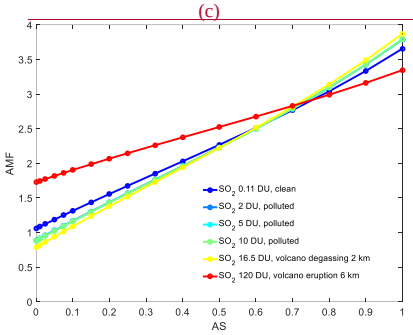

(d)

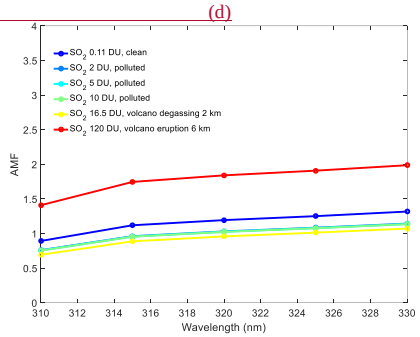

(e)

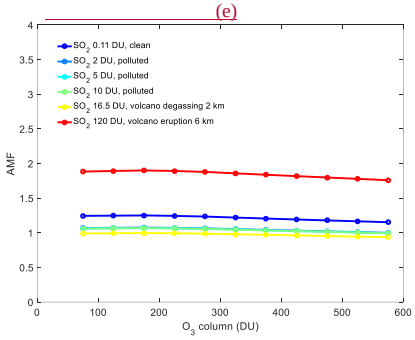

(f)

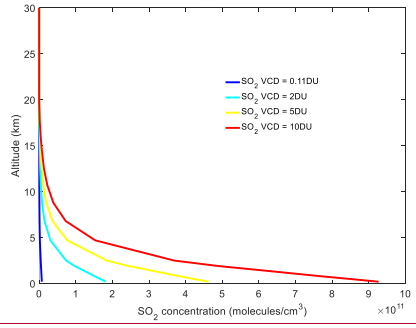

(g)

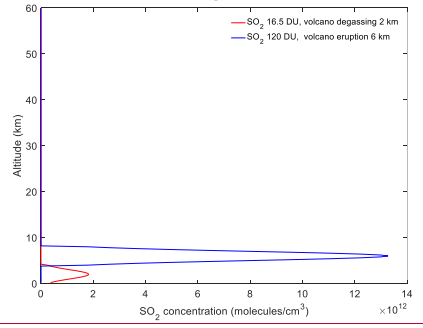

Figure 22: Dependence of AMF on SZA (a), VZA (b), AS (c), Wavelength (d), O_3 column (e), and SO_2 profiles. AMFs are calculated with SCIATRAN Box-AMFs using assumed SO_2 profiles. (f) Assumed SO_2 profiles corresponding to clean

带格式的: 居中

带格式的: 字体: 小五, 加粗

带格式的: 字体: 小五, 加粗

带格式的: 字体: 小五, 加粗

带格式的: 下标

带格式的: 下标

带格式的: 下标

conditions, low, medium, and high anthropogenic SO_2 emissions; (g) Assumed SO_2 profiles corresponding to volcanic degassing with plume heights around 2 km, and volcanic eruption with plume heights around 6 km. The default SCIATRAN settings for Box-AMF calculation are as follows: wavelength=320 nm, clear sky, HS=0 km, O_3=275 DU, AS=0.05, SZA=32.9°, VZA=0°, RAA=0°.

5.3 Errors from background offset correction

Background offset correction is essential for the initial SO_2 column retrievals from satellite observations which usually have systematic overestimation or underestimation problems. However, it is hard to get the accurate background offset for SO_2 retrieval of each pixel. In this study, an iterative sliding correction scheme for background offset correction was applied to initial OMS SO_2 retrievals, with the purpose of forcing SO_2 values over clean or low SO_2 emission regions to zero. This approach helps addressing problems such as along-track stripes and cross-track asymmetry. However, the sliding window strategy assumes that pixels with values smaller than the threshold (2 DU) within the sliding window represent zero SO_2 emissions, which may lead to a loss of SO_2 information contained in the low-emission regions. This not only could limit the applicability of the OMS SO_2 product for monitoring anthropogenic emission sources, but also may lead to many negative retrievals of SO_2 column in clean regions. Furthermore, SO_2 retrievals at certain cross-track positions (assumed to be clean near-zero) may exceed the 2 DU threshold, requiring the threshold to be adjusted upwards to achieve a better effect after background offset correction. Therefore, although the current sliding window strategy helps mitigate background errors, it may also affect the accuracy of OMS SO_2 column retrievals.

6 Conclusions and future work

This study utilized TOA reflected radiance data from the Chinese FY3F/OMS-N instrument, launched in August 2023 to retrieve global SO_2 columns with a DOAS approach. Based on the characteristics of the OMS instrument and the performance of its L1 data, specific schemes including solar spectrum selection, spectral soft calibration, and background offset correction were developed to effectively reduce along-track stripes and across-track asymmetry in the initial OMS SO_2 retrievals.

The OMS SO_2 retrievals were compared with TROPOMI DOAS and TROPOMI COBRA SO_2 products in clean oceanic regions, under volcanic eruption conditions, and in anthropogenic emission regions. The comparison results indicate that OMS retrievals show reasonable agreement with TROPOMI products, have good stability in clean oceanic regions and can be used to monitor SO_2 emissions from volcanic eruptions and anthropogenic sources. In selected clean oceanic regions, the SO_2 values of both OMS and TROPOMI follow approximately a normal distribution centered around 0, with most values concentrated between -2 DU and 2 DU. For the Sundhnúkur and Nyamuragira volcanic eruptions, FY3F/OMS SO_2 retrievals successfully capture the spatial distribution and high-concentration plumes of volcanic SO_2, similar to the TROPOMI DOAS and TROPOMI COBRA 7 km SO_2 results. Over the Sundhnúkur volcano, OMS and TROPOMI DOAS show a high

带格式的: 字体: 小五, 加粗, 英语(英国), 检查拼写和语法

带格式的: 字体: (中文) +中文正文 (宋体), 10 磅, (中文) 中文(中国)

带格式的: 正文

删除的内容: This study utilized TOA reflected radiance data from the Chinese FY3F/OMS-N instrument, launched in August 2023 to retrieve global SO_2 columns with a DOAS approach. Based on the characteristics of the OMS instrument and the performance of its L1 data, specific schemes including solar spectrum selection, spectral soft calibration, and background offset correction were developed to effectively reduce along-track stripes and across-track asymmetry in the initial OMS SO_2 retrievals. The OMS SO_2 retrievals were compared with TROPOMI DOAS and TROPOMI COBRA SO_2 products in clean oceanic regions, under volcanic eruption conditions, and in anthropogenic emission regions. The comparison results indicate that OMS retrievals show good stability in clean oceanic regions and have the capability to monitor SO_2 emissions from volcanic eruptions and anthropogenic sources. In particular, for high-latitude regions with large observation angles (Norilsk region), FY3F/OMS can clearly capture the SO_2 plumes from anthropogenic emissions. Overall, with its high spectral and spatial resolution, morning overpass time, daily global coverage, and reliable SO_2 retrieval results, OMS will provide effective data support for monitoring the continuous SO_2 changes from global volcanic eruptions and anthropogenic activities, helping to fill the spatial and temporal gaps in the existing global satellite network.

带格式的: 下标

correlation of ~0.87, and OMS and TROPOMI COBRA reach ~0.76, indicating good overall agreement. However, OMS tends to underestimate SO_2 at high columns (>50 DU) due to saturation in the 312–326 nm fitting window. In anthropogenic emission regions, OMS and TROPOMI SO_2 products show generally good consistency in detecting anthropogenic SO_2 emissions, with correlation coefficients ranging from about 0.5–0.6 over the Persian Gulf and up to 0.91–0.93 over Norilsk. The differences between OMS and TROPOMI SO_2 results may be related to differences in local overpass times, spatial resolution, observation angles, and the L1 and L2 processing algorithms (e.g., differences in L1 radiometric and spectral calibration methods, SO_2 retrieval fitting windows, AMF strategies). Among these, the AMF used in the SO_2 column retrieval is a major contributor to the differences between OMS and TROPOMI SO_2 results. For example, in the case of the Sundhnúkur volcano, the lack of accurate information on the vertical SO_2 profile can lead to discrepancies of more than a factor of two when comparing the OMS and TROPOMI SO_2 results. Random noise and uncertainties from background correction are relevant for low SO_2 scenarios, such as over the Persian Gulf, and lead to scatter in the order of several DU. However, the results for Norilsk demonstrate that under relatively constant emission conditions, good agreement can be achieved with a simple AMF when the satellite overpass times are well matched.

In summary, the agreement between the OMS and TROPOMI measurements is within expectations, taking into account the differences in satellite overpass times and the uncertainties associated with AMF assumptions. With its high spectral and spatial resolution, morning overpass time, daily global coverage, and reliable SO_2 retrieval results, OMS will provide effective data support for monitoring the continuous SO_2 changes from global volcanic eruptions and anthropogenic activities, helping to fill the spatial and temporal gaps in the existing global satellite network.

The current OMS SO_2 retrievals still have several shortcomings that need to be addressed in the future. Due to the lack of a prior SO_2 and temperature profiles, a simplified approach that uses two constant AMF values for typical conditions was applied for the OMS SO_2 conversion from SCD to VCD in this study. More work will be needed to incorporate accurate and satellite-synchronized SO_2 vertical profiles to improve the accuracy of AMF. Another issue that needs to be addressed in the future is the simultaneous retrieval of volcanic eruption heights, which would help improve the accuracy of SO_2 retrievals in volcanic regions. Additionally, the 312–326 nm retrieval fitting window used in the OMS SO_2 product exhibits nonlinear variation in the case of very large SO_2 concentrations, leading to an underestimation of SO_2 columns. In the future, SO_2 retrievals from longer UV wavelength fitting windows varying with SO_2 columns will be incorporated into the operational OMS SO_2 products to mitigate the saturation issue in the case of large volcanic eruptions. Our preliminary strategy for such retrievals is as follows. First, a global SO_2 column retrieval is performed using the 312–326 nm window. Pixels exceeding a threshold (e.g., >50 DU) are flagged as potentially saturated. For these flagged pixels, additional retrievals are conducted using the 325–335 nm and 360–390 nm windows. If the new retrievals are within a reasonable range and exceed the 312–326 nm results, the maximum value from the 325–335 nm or 360–390 nm windows replaces the original retrieval; otherwise, the 312–326 nm retrieval is retained.

Furthermore, although in this study the comparison between OMS SO_2 retrievals and TROPOMI SO_2 products was conducted to demonstrate the capability of OMS SO_2 retrievals, synchronous and high-quality ground-based or airborne

删除的内容: or nonlinear spectral fitting or correction factors

measurements remain crucial for validating the accuracy of OMS SO_2 retrievals. In the future, ground-based and airborne experiments need to be conducted to provide accurate ground-based or airborne data for the validation of OMS SO_2 retrievals.

Author contribution

Huanhuan Yan: Drafting, data processing, and plotting; Andreas Richter: Revision, research methodology and content suggestions, and English polishing; Xingying Zhang: Suggestions on revision and research direction; Anja Schönhardt: Discussion and suggestions on the Ring effect; Thomas Visarius: Discussion and suggestions on AMF calculation.

Data Availability

The SO_2 data produced in this study is available from the authors on request. FY3F/OMS-N L1 data can be downloaded from the website http://data.nsmc.org.cn/DataPortal/en/home/index.html. TROPOMI DOAS SO_2 data is available via the Copernicus Data Space Ecosystem (https://browser.dataspace.copernicus.eu/). TROPOMI COBRA SO_2 data is available via the PAL system (https://data-portal.s5p-pal.com/products/so2cbr.html).

Acknowledgements

This study has been supported by the National Key Research and Development Program of China under Grant 2022YFB3904801. The authors wish to thank the many scientists and engineers from FY3F/OMS L1 team, TROPOMI team, and the Institute of Environmental Physics at the University of Bremen. The authors also acknowledge the use of ChatGPT for improving the English of the manuscript.

References

Bauduin, S., Clarisse, L., Clerbaux, C., Hurtmans, D., and Coheur, P. F.: IASI observations of sulfur dioxide (SO_2) in the boundary layer of Norilsk, J Geophys Res-Atmos, 119, 4253-4263, 2014.

Boersma, K., Eskes, H., and Brinksma, E.: Error analysis for tropospheric NO_2 retrieval from space, J Geophys Res-Atmos, 109, 2004.

Bogumil, K., Orphal, J., Homann, T., Voigt, S., Spietz, P., Fleischmann, O. C., Vogel, A., Hartmann, M., Kromminga, H., Bovensmann, H., Frerick, J., and Burrows, J. P.: Measurements of molecular absorption spectra with the SCIAMACHY pre-flight model: instrument characterization and reference data for atmospheric remote-sensing in the 230–2380 nm region, Journal of Photochemistry and Photobiology A: Chemistry, 157, 167-184, 10.1016/s1010-6030(03)00062-5, 2003.

Burrows, J. P., Weber, M., Buchwitz, M., Rozanov, V., Ladstatter-Weissenmayer, A., Richter, A., DeBeek, R., Hoogen, R., Bramstedt, K., Eichmann, K. U., and Eisinger, M.: The global ozone monitoring experiment (GOME): Mission concept and first scientific results, J Atmos Sci, 56, 151-175, Doi 10.1175/1520-0469(1999)056<0151:Tgomeg>2.0.Co;2, 1999.

Carn, S. A., Krueger, A. J., Krotkov, N. A., Yang, K., and Evans, K.: Tracking volcanic sulfur dioxide clouds for aviation hazard mitigation, Nat Hazards, 51, 325-343, DOI 10.1007/s11069-008-9228-4, 2009.

Carn, S. A., Krueger, A. J., Krotkov, N. A., Yang, K., and Levelt, P. F.: Sulfur dioxide emissions from Peruvian copper smelters detected by the Ozone Monitoring Instrument, Geophys Res Lett, 34, 1093-1101, 10.1029/2006gl029020, 2007.

Carn, S. A., Strow, L. L., de Souza-Machado, S., Edmonds, Y., and Hannon, S.: Quantifying tropospheric volcanic emissions with AIRS: The 2002 eruption of Mt. Etna (Italy), Geophys Res Lett, 32, Artn L02301 Doi 10.1029/2004gl021034, 2005.

Chance, K. V. and Spurr, R. J.: Ring effect studies: Rayleigh scattering, including molecular parameters for rotational Raman scattering, and the Fraunhofer spectrum, Appl Optics, 36, 5224-5230, 1997.

Chen, L., Han, D., Tao, J., and Su, L.: Overview of tropospheric NO_2 vertical column density retrieval from space measurement, Journal of Remote Sensing, 13, 343-360, 2009.

Chen, L., Shang, H., Fan, M., Tao, J., Husi, L., Zhang, Y., Wang, H., Cheng, L., Zhang, X., and Wei, L.: Mission overview of the GF-5 satellite for atmospheric parameter monitoring, National Remote Sensing Bulletin, 25, 1917-1931, 2021.

Coddington, O. M., Richard, E. C., Harber, D., Pilewskie, P., Woods, T. N., Chance, K., Liu, X., and Sun, K.: The TSIS-1 hybrid solar reference spectrum, Geophys Res Lett, 48, e2020GL091709, 2021.

Cofano, A., Cigna, F., Santamaria Amato, L., Siciliani de Cumis, M., and Tapete, D.: Exploiting Sentinel-5P TROPOMI and ground sensor data for the detection of volcanic SO_2 plumes and activity in 2018–2021 at Stromboli, Italy, Sensors-Basel, 21, 6991, 2021.

Corradino, C., Jouve, P., La Spina, A., and Del Negro, C.: Monitoring Earth's atmosphere with Sentinel-5 TROPOMI and Artificial Intelligence: Quantifying volcanic SO_2 emissions, Remote Sens Environ, 315, 114463, 2024.

Cullis, C. F. and Hirschler, M. M.: Atmospheric Sulfur - Natural and Man-Made Sources, Atmos Environ, 14, 1263-1278, Doi 10.1016/0004-6981(80)90228-0, 1980.

Eisinger, M. and Burrows, J. P.: Tropospheric sulfur dioxide observed by the ERS-2 GOME instrument, Geophys Res Lett, 25, 4177-4180, Doi 10.1029/1998gl900128, 1998.

Finlayson-Pitts, B. J. and Pitts Jr, J. N.: Chemistry of the upper and lower atmosphere: theory, experiments, and applications, Elsevier1999.

Fioletov, V., McLinden, C. A., Griffin, D., Theys, N., Loyola, D. G., Hedelt, P., Krotkov, N. A., and Li, C.: Anthropogenic and volcanic point source SO_2 emissions derived from TROPOMI on board Sentinel-5 Precursor: first results, Atmos Chem Phys, 20, 5591-5607, 2020.

Fioletov, V., McLinden, C., Krotkov, N., Yang, K., Loyola, D., Valks, P., Theys, N., Van Roozendael, M., Nowlan, C., and Chance, K.: Application of OMI, SCIAMACHY, and GOME-2 satellite SO_2 retrievals for detection of large emission

sources, J Geophys Res-Atmos, 118, 11,399-311,418, 2013.

Fish, D. and Jones, R.: Rotational Raman scattering and the ring effect in zenith-sky spectra, Geophys Res Lett, 22, 811-814, 1995.

Flynn, L. E., Seftor, C. J., Larsen, J. C., and Xu, P.: The Ozone Mapping and Profiler Suite, 2006.

Global Volcanism Program, 2024. Report on Nyamuragira (DR Congo) (Sennert, S, ed.). Weekly Volcanic Activity Report, 6 November-12 November 2024. Smithsonian Institution and US Geological Survey.

Global Volcanism Program, 2024. Report on Reykjanes (Iceland) (Sennert, S, ed.). Weekly Volcanic Activity Report, 21 August-27 August 2024. Smithsonian Institution and US Geological Survey.

Gottwald, M. and Bovensmann, H.: SCIAMACHY-Exploring the changing Earth's Atmosphere, Springer Science & Business Media2010.

Grainger, J. and Ring, J.: Anomalous Fraunhofer line profiles, Nature, 193, 762-762, 1962.

Heue, K. P., Brenninkmeijer, C. A. M., Wagner, T., Mies, K., Dix, B., Frieß, U., Martinsson, B. G., Slemr, F., and van Velthoven, P. F. J.: Observations of the 2008 Kasatochi volcanic SO_2 plume by CARIBIC aircraft DOAS and the GOME-2 satellite, Atmos Chem Phys, 10, 4699-4713, 10.5194/acp-10-4699-2010, 2010.

Khokhar, M. F., Frankenberg, C., Van Roozendael, M., Beirle, S., Kühl, S., Richter, A., Platt, U., and Wagner, T.: Satellite observations of atmospheric SO_2 from volcanic eruptions during the time-period of 1996–2002, Adv Space Res, 36, 879-887, 10.1016/j.asr.2005.04.114, 2005.

Kleipool, Q., Dobber, M., de Haan, J., and Levelt, P.: Earth surface reflectance climatology from 3 years of OMI data, J Geophys Res-Atmos, 113, 2008.

Krotkov, N. A., Carn, S. A., Krueger, A. J., Bhartia, P. K., and Yang, K.: Band residual difference algorithm for retrieval of SO_2 from the aura Ozone Monitoring Instrument (OMI), IEEE Trans. Geosci. Remote Sensing, 44, 1259-1266, Doi 10.1109/Tgrs.2005.861932, 2006.

Krotkov, N. A., McLinden, C. A., Li, C., Lamsal, L. N., Celarier, E. A., Marchenko, S. V., Swartz, W. H., Bucsela, E. J., Joiner, J., and Duncan, B. N.: Aura OMI observations of regional SO_2 and NO_2 pollution changes from 2005 to 2015, Atmos Chem Phys, 16, 4605-4629, 2016.

Krotkov, N. A., McClure, B., Dickerson, R. R., Carn, S. A., Li, C., Bhartia, P. K., Yang, K., Krueger, A. J., Li, Z. Q., Levelt, P. F., Chen, H. B., Wang, P. C., and Lu, D. R.: Validation of SO_2 retrievals from the Ozone Monitoring Instrument over NE China, J Geophys Res-Atmos, 113, 259-269, Artn D16s40
Doi 10.1029/2007jd008818, 2008.

Krueger, A. J.: Sighting of El Chichón Sulfur Dioxide Clouds with the Nimbus 7 Total Ozone Mapping Spectrometer, Science, 220, 1377-1379, DOI 10.1126/science.220.4604.1377, 1983.

Kuttippurath, J., Patel, V. K., Pathak, M., and Singh, A.: Improvements in SO_2 pollution in India: role of technology and environmental regulations, Environ Sci Pollut R, 29, 78637-78649, 2022.

Lee, C., Martin, R. V., van Donkelaar, A., O'Byrne, G., Krotkov, N., Richter, A., Huey, L. G., and Holloway, J. S.: Retrieval

of vertical columns of sulfur dioxide from SCIAMACHY and OMI: Air mass factor algorithm development, validation, and error analysis, J Geophys Res, 114, 10.1029/2009jd012123, 2009.

Levelt, P. F., Van den Oord, G. H. J., Dobber, M. R., Malkki, A., Visser, H., de Vries, J., Stammes, P., Lundell, J. O. V., and Saari, H.: The Ozone Monitoring Instrument, IEEE Trans. Geosci. Remote Sensing, 44, 1093-1101, Doi 10.1109/Tgrs.2006.872333, 2006.

Li, C., Joiner, J., Krotkov, N. A., and Bhartia, P. K.: A fast and sensitive new satellite SO_2 retrieval algorithm based on principal component analysis: Application to the ozone monitoring instrument, Geophys Res Lett, 40, 6314-6318, 2013.

Lorente, A., Folkert Boersma, K., Yu, H., Dörner, S., Hilboll, A., Richter, A., Liu, M., Lamsal, L. N., Barkley, M., and De Smedt, I.: Structural uncertainty in air mass factor calculation for NO_2 and HCHO satellite retrievals, Atmos Meas Tech, 10, 759-782, 2017.

Mardani, M., Nowrouzi, M., and Abyar, H.: Assessing the environmental impact of offshore flares in the Persian Gulf: A comprehensive analysis of SO_2 emissions, Advances in Environmental Technology, 11, 63-74, 2025.

Mccormick, M. P., Thomason, L. W., and Trepte, C. R.: Atmospheric effects of the Mt. Pinatubo eruption, Nature, 373, 399-404, Doi 10.1038/373399a0, 1995.

Miller, T., P. and Casadevall, T., J.: Volcanic ash hazards to aviation, in: Encyclopedia of Volcanoes, edited by: Sigurdsson, H., Academic Press, San Diego, 915-930, 2000.

Munro, R., Eisinger, M., Anderson, C., Callies, J., Corpaccioli, E., Lang, R., Lefebvre, A., Livschitz, Y., and Albiñana, A. P.: GOME-2 on MetOp, Proc. of The 2006 EUMETSAT Meteorological Satellite Conference, Helsinki, Finland, 12—16 June, 12-16,

Newhall, C. G. and Self, S.: The volcanic explosivity index (VEI) an estimate of explosive magnitude for historical volcanism, Journal of Geophysical Research: Oceans, 87, 1231-1238, 1982.

Nowlan, C., Liu, X., Chance, K., Cai, Z., Kurosu, T., Lee, C., and Martin, R.: Retrievals of sulfur dioxide from the Global Ozone Monitoring Experiment 2 (GOME-2) using an optimal estimation approach: Algorithm and initial validation, J Geophys Res-Atmos, 116, 2011.

Palmer, P. I., Jacob, D. J., Chance, K., Martin, R. V., Spurr, R. J., Kurosu, T. P., Bey, I., Yantosca, R., Fiore, A., and Li, Q.: Air mass factor formulation for spectroscopic measurements from satellites: Application to formaldehyde retrievals from the Global Ozone Monitoring Experiment, J Geophys Res-Atmos, 106, 14539-14550, 2001.

Platt, U. and Stutz, J.: Differential Optical Absorption Spectroscopy: Principles and Applications, Physics of Earth and Space Environments, Springer, Verlag Berlin Heidelberg, 593 pp., 10.1007/978-3-540-75776-4 2008.

Richter, A.: Algorithm Theoretical Basis Document for the GOME-2 Rapid Volcanic SO_2 product, SAVAA project.[Available at https://www.iup.uni-bremen.de/doas/so2_alerts/gome2_so2_atbd_091005.pdf], 2009.

Richter, A., Wittrock, F., and Burrows, J. P.: SO_2 measurements with SCIAMACHY, Proc. Atmospheric Science Conference, Frascati, Italy, 8 -12 May, 8-12,

Rozanov, A., Rozanov, V., Buchwitz, M., Kokhanovsky, A., and Burrows, J.: SCIATRAN 2.0–A new radiative transfer

model for geophysical applications in the 175–2400 nm spectral region, Adv Space Res, 36, 1015-1019, 2005.

Seinfeld, J. H. and Pandis, S. N.: Atmospheric chemistry and physics: from air pollution to climate change, John Wiley & Sons2016.

Sinnhuber, B.-M., Sheode, N., Sinnhuber, M., Chipperfield, M., and Feng, W.: The contribution of anthropogenic bromine emissions to past stratospheric ozone trends: a modelling study, Atmos Chem Phys, 9, 2863-2871, 2009.

Sioris, C. E. and Evans, W. F.: Filling in of Fraunhofer and gas-absorption lines in sky spectra as caused by rotational Raman scattering, Appl Optics, 38, 2706-2713, 1999.

Theys, N., De Smedt, I., Yu, H., Danckaert, T., van Gent, J., Hörmann, C., Wagner, T., Hedelt, P., Bauer, H., and Romahn, F.: Sulfur dioxide retrievals from TROPOMI onboard Sentinel-5 Precursor: algorithm theoretical basis, Atmos Meas Tech, 10, 119-153, 2017.

Theys, N., Hedelt, P., De Smedt, I., Lerot, C., Yu, H., Vlietinck, J., Pedergnana, M., Arellano, S., Galle, B., and Fernandez, D.: Global monitoring of volcanic SO_2 degassing with unprecedented resolution from TROPOMI onboard Sentinel-5 Precursor, Sci Rep-Uk, 9, 2643, 2019.

Theys, N., Fioletov, V., Li, C., De Smedt, I., Lerot, C., McLinden, C., Krotkov, N., Griffin, D., Clarisse, L., Hedelt, P., Loyola, D., Wagner, T., Kumar, V., Innes, A., Ribas, R., Hendrick, F., Vlietinck, J., Brenot, H., and Van Roozendael, M.: A sulfur dioxide Covariance-Based Retrieval Algorithm (COBRA): application to TROPOMI reveals new emission sources, Atmos. Chem. Phys., 21, 16727-16744, 10.5194/acp-21-16727-2021, 2021.

Tilstra, L. G., de Graaf, M., Trees, V. J., Litvinov, P., Dubovik, O., and Stammes, P.: A directional surface reflectance climatology determined from TROPOMI observations, Atmos Meas Tech, 17, 2235-2256, 2024.

Twomey, S.: The Influence of Pollution on the Shortwave Albedo of Clouds, J Atmos Sci, 34, 1149-1152, 10.1175/1520-0469(1977)034<1149:TIOPOT>2.0.CO;2, 1977.

van Geffen, J. H. and van Oss, R. F.: Wavelength calibration of spectra measured by the Global Ozone Monitoring Experiment by use of a high-resolution reference spectrum, Appl Optics, 42, 2739-2753, 2003.

Vandaele, A. C., Hermans, C., and Fally, S.: Fourier transform measurements of SO_2 absorption cross sections: II. Temperature dependence in the 29 000-44 000 cm(-1) (227-345 nm) region, J Quant Spectrosc Ra, 110, 2115-2126, DOI 10.1016/j.jqsrt.2009.05.006, 2009.

Veefkind, J., Aben, I., McMullan, K., Förster, H., De Vries, J., Otter, G., Claas, J., Eskes, H., De Haan, J., and Kleipool, Q.: TROPOMI on the ESA Sentinel-5 Precursor: A GMES mission for global observations of the atmospheric composition for climate, air quality and ozone layer applications, Remote Sens Environ, 120, 70-83, 2012.

Voors, R., De Vries, J., Bhatti, I. S., Lobb, D., Wood, T., Nick, V. D. V., Aben, I., and Veefkind, P.: TROPOMI, the Sentinel 5 precursor instrument for air quality and climate observations: status of the current design, Society of Photo-optical Instrumentation Engineers,

Vountas, M., Rozanov, V., and Burrows, J.: Ring effect: Impact of rotational Raman scattering on radiative transfer in Earth's atmosphere, Journal of Quantitative Spectroscopy and Radiative Transfer, 60, 943-961, 1998.

Wagner, T., Burrows, J., Deutschmann, T., Dix, B., Von Friedeburg, C., Frieß, U., Hendrick, F., Heue, K.-P., Irie, H., Iwabuchi, H., Kanaya, Y., Keller, J., McLinden, C. A., Oetjen, H., Palazzi, E., Petritoli, A., Platt, U., Postylyakov, O., Pukite, J., Richter, A., van Roozendael, M., Rozanov, A., Rozanov, V., Sinreich, R., Sanghavi, S., and Wittrock, F.: Comparison of box-air-mass-factors and radiances for Multiple-Axis Differential Optical Absorption Spectroscopy (MAX-DOAS) geometries calculated from different UV/visible radiative transfer models, Atmos Chem Phys, 7, 1809-1833, 2007.

Wang, C., Wang, T., Wang, P., and Wang, W.: Assessment of the performance of TROPOMI NO_2 and SO_2 data products in the North China Plain: comparison, correction and application, Remote Sens-Basel, 14, 214, 2022.

Wang, Q., Wang, Y., Xu, N., Mao, J., Sun, L., Shi, E., Hu, X., Chen, L., Yang, Z., and Si, F.: Preflight Spectral Calibration of the Ozone Monitoring Suite-Nadir on FengYun 3F Satellite, Remote Sens-Basel, 16, 1538, 2024.

Yan, H., Wang, W., and Chen, L.: Temperature effects on the retrieval of SO_2 from ultraviolet satellite observations, Remote Sensing of the Atmosphere, Clouds, and Precipitation V, 379-386,

Yan, H., Wang, H., Wang, W., and Zhang, X.: Volcanic SO_2 retrieved from GF-5 Environmental trace gas Monitoring Instrument, National Remote Sensing Bulletin, 25, 2326-2338, 10.11834/jrs.20210303, 2021.

Yan, H., Li, X., Wang, W., Zhang, X., Chen, L., Han, D., Yu, C., and Gao, L.: Comparison of SO_2 column retrievals from BRD and DOAS algorithms, Science China Earth Sciences, 60, 1694-1706, 2017.

Yang, K., Dickerson, R. R., Carn, S. A., Ge, C., and Wang, J.: First observations of SO_2 from the satellite Suomi NPP OMPS: Widespread air pollution events over China, Geophys Res Lett, 40, 4957-4962, 2013.

Yang, K., Krotkov, N. A., Krueger, A. J., Carn, S. A., Bhartia, P. K., and Levelt, P. F.: Retrieval of large volcanic SO_2 columns from the Aura Ozone Monitoring Instrument: Comparison and limitations, J Geophys Res, 112, D24S43, doi: 10.1029/2007JD008825, 2007.

Yang, K., Krotkov, N. A., Krueger, A. J., Carn, S. A., Bhartia, P. K., and Levelt, P. F.: Improving retrieval of volcanic sulfur dioxide from backscattered UV satellite observations, Geophys Res Lett, 36, 2009.

Yang, K., Liu, X., Bhartia, P. K., Krotkov, N. A., Carn, S. A., Hughes, E. J., Krueger, A. J., Spurr, R. J., and Trahan, S. G.: Direct retrieval of sulfur dioxide amount and altitude from spaceborne hyperspectral UV measurements: Theory and application, J Geophys Res-Atmos, 115, 2010.

Zhao, M., Si, F., Wang, Y., Zhou, H., Wang, S., Jiang, Y., and Liu, W.: First Year On-Orbit Calibration of the Chinese Environmental Trace Gas Monitoring Instrument Onboard GaoFen-5, IEEE Trans. Geosci. Remote Sensing, 58, 8531-8540, 2020.